Title

Modeling of fluid injection-induced fault reactivation using coupled fluid flow and mechanical interface model

Authors
Park, Jung-Wook
Guglielmi, Yves
Graupner, Bastian
et al.

Publication Date
2020-08-01

DOI
10.1016/j.ijrmms.2020.104373

Peer reviewed

Modeling of Fluid Injection-Induced Fault Reactivation Using Coupled Fluid Flow and Mechanical Interface Model

Jung-Wook Park[1,*], Yves Guglielmi[2], Bastian Graupner[3], Jonny Rutqvist[2], Taehyun Kim[1], Eui-Seob Park[1], Changsoo Lee[4]

[1] Korea Institute of Geoscience and Mineral Resources (KIGAM), 124 Gwahak-ro, Yuseong-gu, Daejeon 34132, Republic of Korea

[2] Lawrence Berkeley National Laboratory (LBNL), Berkeley, CA 94720, USA

[3] Swiss Federal Nuclear Safety Inspectorate (ENSI), 5200 Brugg, Switzerland

[4] Korea Atomic Energy Research Institute (KAERI), 111 Daedeok-daero, 989 beon-gil, Yuseong-gu, Daejeon 34057, Republic of Korea

* Corresponding author
Jung-Wook Park
E-mail: jwpark@kigam.re.kr
Telephone: +82-42-868-3246
Fax: +82-42-868-3416

Abstract

The present study is aimed at developing a numerical model to reproduce coupled hydro-mechanical processes associated with fault reactivation by fluid injection in low permeability rock, as part of the DECOVALEX-2019 project Task B. We proposed a modeling approach for simulating the processes using the TOUGH-FLAC simulator, and modeled a fault reactivation experiment conducted at Mont Terri Rock Laboratory in Switzerland. The first step of the study involved benchmark calculations considering a simplified fault plane and geometry. Fluid flow along a fault was modeled using elements of aperture-sized thickness on the basis of Darcy's law and the cubic law in TOUGH2, whereas the mechanical behavior of a single fault was represented by zero-thickness interface elements in FLAC3D upon which a slip and/or separation is allowed. A methodology to connect a TOUGH2 volume element to a FLAC3D interface element was developed for handling the hydro-mechanical interactions on the fault during fluid injection. Two different fault models for describing the evolutions of hydraulic aperture by elastic fracture opening and failure-induced aperture increase were considered in the benchmark calculations. In the coupling process, the changes in geometrical features and hydrological properties induced by mechanical deformation were continuously updated. The transient responses of the fault and host rock to stepwise pressurization were examined during the simulation. The hydro-mechanical behavior, including the injection flow rate, pressure distribution around the borehole, stress conditions, and displacements in normal and shear directions were monitored in the surrounding rock and along the fault. The results of benchmark calculations suggest that the developed model reasonably represents the hydro-mechanical behavior of a fault and the surrounding rock. This modeling approach was applied to the fault reactivation experiment of the Mont Terri Rock Laboratory. In this interpretive modeling, a parametric study was conducted to examine the effects of input parameters regarding in situ stress and fault properties on the hydro-mechanical responses of the fault to water injection. Then, an optimal parameter set to reproduce the field experiment results was chosen by trial-and-error. The injection flow rate and pressure response during fault reactivation closely matched those obtained at the site, which indicates the capability of the model to appropriately capture the progressive pathway evolution during fault reactivation tests at the site. The anchor displacements were overestimated by the model, but a fair agreement was obtained in terms of the order of magnitude and the variation tendency.

Keywords: Fault Reactivation, Water Injection, DECOVALEX-2019, Mont Terri Rock Laboratory, TOUGH-FLAC, Coupled Hydro-Mechanical Analysis

1. Introduction

The importance of an appropriate assessment on the fault reactivation by fluid injection into rock is increasingly recognized, as promoted by rising demands for the technologies associated with geological CO2 sequestration, shale gas development, enhanced geothermal systems, and enhanced oil/gas recovery. Injected fluid changes the prevailing stress state in a reservoir and pre-existing faults and fractures, and thus potentially triggers fault slip and seismicity. Fault activation may also be induced associated with deep geological nuclear waste disposal, especially in low permeability rock, where thermally driven fluid pressure increases (thermal pressurization) and pressure increases due to gas generation could be significant. The fault reactivation process is a combination of hydrological and mechanical interactions, such as hydraulic aperture evolution, hydrological properties change, effective stress induction, and mechanical strength degradation. Development of technologies for understanding and estimating the behavior is essential in ensuring safe and reliable operation of relevant energy facilities and gaining public acceptance of potential hazards such as induced seismicity.

The fault reactivation potential can be assessed using analytical and numerical methods. An analytical method estimates the possibility and extent of fault failure from theoretical calculations of fault plane stress states, which generally relies on the Coulomb failure criterion for shear strength.[1] The fault stability and fault slip critical pressure threshold can be determined depending on fault direction based on a simple approach.[2, 3] Analytical methods, however, imply many assumptions and simplifications, and thus have interpretation limitations for the complicated hydro-mechanical process in faults and reservoirs, although they are useful tools in the preliminary design stage.

Numerical methods can offer a viable alternative for more comprehensive analysis on the fault reactivation risk. For example, numerical modeling enables consideration of the initial and induced stresses, progressive changes of hydrological and mechanical properties, and failure processes. Mechanically, fault representation by numerical approaches can be classified into two categories: continuum and discontinuum approaches, depending on whether the fault is modeled as a continuum material or as a discontinuity. In the former approach, which is widely employed in geomechanics, the fault is modeled as layer of finite thickness in a continuum model (finite element method or finite difference method).[4–7] The fault is assumed to have the same mechanical responses as an equivalent continuum, and then relationships can be derived between fault properties and equivalent continuum properties. The latter approach defines a fault as a zero-thickness discontinuity (interface in continuum model or a series of contact formations in the discrete element method).[8–15] This model is available to represent fault surfaces as distinct planes upon which slip and/or separation are allowed based on shear and tensile failure criteria. Cappa and Rutqvist[10] showed that different fault modeling approaches using finite-thickness elements and zero-thickness interfaces produced similar results, and therefore, the least complex approach using finite thickness elements was appropriate for fault representation from a comparative simulation on fault reactivation induced by CO2 injection. However, the study was based on the one-way coupled hydro-mechanical analysis not considering hydraulic aperture change due to mechanical deformation. It is still questioned whether the finite thickness element modeling with equivalent properties can adequately reproduce the effect of continually changing hydraulic aperture in a two-way coupled analysis.

Both modeling approaches have limitations and assumptions for conceptualization of fault behavior. The choice is dependent upon the scale of interest, required properties of the associated model, and conditions of rock mass and discontinuities.[1, 16] In the continuum model, the failure state is characterized by plastic strain and the displacement across a fault is a continuous approximation. Thus, the results can be dependent on grid resolution and may be unrealistic when predicting large displacement. In field-scale problems where the fault thickness is negligible compared to the scale of interest, it may also be challenging to generate a thin layer that approximates the fault. To explicitly represent fault behavior in large-scale problems, a single discontinuity may be preferable, although the discontinuum approach requires cautious selection of fault stiffness to avoid numerical instability.

The present study is aimed at developing a numerical method to reproduce the hydro-mechanical behavior of a fault by fluid injection using the TOUGH-FLAC simulator as suggested by Rutqvist et al.[17] We propose a modeling approach through benchmark calculations with two different fault models, and demonstrate its applicability by reproducing the field experiment results obtained at the Mont Terri Rock Laboratory in Switzerland. This study has been conducted as part of the DECOVALEX (Development of Coupled models and their VALidation against EXperiments) project, an international research and model comparison collaboration for understanding and modeling of coupled thermo-hydro-mechanical-chemical processes in geological systems.[18] The current phase is DECOVALEX-2019 running from 2016 through 2019, and this study falls under Task B entitled 'Modeling the induced slip of a fault in argillaceous rock'. Seven modeling teams participate in analyzing fluid injection tests using different modeling approaches.[19] Task B consists of three steps related to modeling of fault reactivation experiments performed at the Mont Terri Rock Laboratory. Step 1 is the model inception based on the benchmark calculation of a single fault plane, and Step 2 and Step 3 are for the interpretive modeling of fault reactivation experiments at the site.

In this study, we describe our Step 1 and Step 2 research results. Section 2 introduces the developed numerical model and Section 3 presents the results of Step 1, the benchmark calculations. Section 4 discusses the results of Step 2, the application of the developed model to a minor fault slip experiment at the Mont Terri Rock Laboratory, which is then followed by a few conclusions.

2. Development of numerical model using the TOUGH-FLAC simulator

2.1 Description of benchmark simulations

The objective of DECOVALEX-2019 Task B is to develop, compare, and validate numerical models for simulating fault reactivation induced by fluid injection.[19] Step 1 of Task B is a model inception with well-defined models based on a simplified representation of the fault plane and geometry. The key concerns focus on the coupling between the fracture hydraulic properties and the slip-induced displacement during fault reactivation. Therefore, an appropriate estimation of progressive evolution of hydraulic aperture is the most critical factor determining the coupled hydro-mechanical process occurring along the fault.

The host rock is represented as a box-shaped region with a side length of 20 m containing a fault dipping 65° in its center. The estimated properties for Opalinus Clay with a minor fault and the injection scheme used in the field experiment on a minor fault are applied to the benchmark simulations. Fig. 1 shows the injection pressure scheme consisting of nine steps: the pressure is increased up to 6.302 MPa until the eighth step, and then decreased to 3.382 MPa for the last step.

In the benchmark simulation, it is assumed that the host rock is impermeable and that the injected water flows only through the fault. Two different fault models, FM1 and FM2, are considered to handle the hydraulic aperture evolution. The main difference between the models is that the fracture is closed until failure occurs in the former, while it is initially open in the latter. The model FM1 is based on the modeling experience with fault reactivation tests conducted at the Tournemire in Southern France.[20] In their study, analysis of measured data indicated that the hydraulic aperture increase was higher than the approximation by the dilation during slip. In FM1, it is assumed that the fluid flow only occurs through the fractured (open) parts of the fault, which is initially closed before the stress state reaches the shear or tensile failure criterion. After failure, an open part is created, and an irreversible aperture called ‘creation aperture’ is assigned as its current hydraulic aperture. The open part can thereafter experience elastic normal displacement in response to effective normal stress. Note that the fault is assumed to be initially open and permeable around the injection well to a distance of 0.5 m. This implies the existence of an initially created fracture. The hydraulic aperture of FM1 can be formularized into Eq. 1:

$$\begin{aligned} b_h &= \Delta b_{he} + b_{hc} && r_f \le 0.5\ m \\ b_h &= 0 && r_f > 0.5\ m,\ \textit{before failure} \\ b_h &= \Delta b_{he} + b_{hc} && r_f > 0.5\ m,\ \textit{after failure} \end{aligned} \tag{1}$$

where b_h is the hydraulic aperture of fault, Δb_{he} is elastic deformation in normal direction, b_{hc} is the creation aperture induced by tensile or shear failure, and r_f is radius of the circular zone corresponding to the initially created fracture.

The elastic deformation is determined by the effective normal stress increment and the normal stiffness of the fault.

$$\Delta b_{he} = \frac{\Delta \sigma'_n}{K_n} \tag{2}$$

where $\Delta\sigma'_n$ is the effective normal stress increment and K_n is the normal stiffness of the fault.

Model FM2 is a more conventional approach in which hydraulic aperture is assumed to be consistent with mechanical aperture. FM2 consists of a non-zero initial aperture, elastic normal deformation, and slip-induced dilation. The hydraulic aperture is expressed as Eq. 3.

$$b_h = b_{hi} + \Delta b_{he} + \Delta b_{hs} \tag{3}$$

where b_{hi} is the initial aperture and Δb_{hs} is the aperture induced by shear dilation along the fault zone.

The dilation occurring at slip is approximated as a linear equation using the dilation angle, ψ, and shear displacement increment, Δu_s.

$$\Delta b_{hs} = \Delta u_s \tan\psi \tag{4}$$

In FM1, initially b_{hi} is zero and b_{hc} is 28 μm within a distance of 0.5 m from the injection. After shear or tensile failure occurs, the hydraulic aperture is determined by the elastic deformation and 28-μm creation aperture. In FM2, b_{hi} is 10 μm, and Δb_{hs} is determined by a dilation angle of 10° after shear rupture initiation. The host rock and fault are considered to be elastic and elastic-perfectly plastic, respectively. Table 1 lists the input parameters of the host rock, fluid, and fault zone.

2.2 Numerical model

In the present study, we adopted the TOUGH-FLAC simulator, which was initially developed by Rutqvist et al.[17] as pragmatic approach for modeling thermal-hydrological-mechanical (THM) processes in porous and fractured geological media. The TOUGH-FLAC simulator is based on linking two well-established existing codes, TOUGH2[21] and FLAC3D[22]. The respective merits of both codes have allowed the TOUGH-FLAC simulator to be widely applied to many THM problems in geological media, such as CO2 injection, natural gas production, geothermal reservoir engineering, nuclear waste disposal and energy storage systems in rock caverns.[7, 23–30] In this approach, TOUGH2 and FLAC3D are executed sequentially. The TOUGH2 calculates multi-phase pressures and temperatures and transfers the results to the FLAC3D, and then the FLAC3D conducts a quasi-static mechanical analysis at the TOUGH2 time step and updates the changes in input parameters for the next calculation in TOUGH2. The procedures to link the two codes are provided in detail in Ref. **17.**

Fig. 2 shows the benchmark model domain and mesh for the mechanical model built in FLAC3D. P1 is the injection point, and P2 and P3 are the monitoring points for mechanical and hydrological responses to water injection. The monitoring points are located 1.5 m from the injection point in the strike and dip directions of the fault. The relative displacements between two anchors are monitored during the simulation. The anchors are installed at the fault hanging wall and footwall, respectively, and spaced at a vertical distance of 0.5 m. The host rock and fault are characterized by elastic and elastic-perfectly plastic models, respectively, in FLAC3D. A zero-thickness mechanical interface model upon which slips and/or separation are allowed represents a single fault. The interface model is available to simulate distinct interfaces between zone elements, thereby simulating the presence of faults, joints, or fictional boundaries. If an interface element is defined and attached on a zone element face (host face), interface nodes are automatically created at every interface element vertex. The fundamental contact relation is defined between the interface node and its contacting zone element face (target face), and characterized by normal and shear stiffnesses and sliding properties.[22] The shear and tensile failure are characterized by Coulomb shear strength and tensile strength. Based on an effective stress calculation, a slip and/or tensile separation can occur along the interface elements.

Generally, the modeling approach using the TOUGH-FLAC simulator employs a compatible numerical mesh for both codes. In the present study, however, it is assumed that the host rock is impermeable and its poroelastic responses to water injection are negligible compared to the processes in fault, and thus the flow analysis and hydro-mechanical coupling for the host rock are not taken into account in the simulations. For this reason, only the flow along the fault was simulated in TOUGH2. By taking advantage of flexibility of space discretization in TOUGH2, we directly generated a very thin layer in which element thickness was identical to the real size of fault hydraulic aperture with a uniform porosity value of 1.0. The mesh included some non-orthogonal connections between two adjacent interface elements, which arose from the procedure to install triangular interface elements on quadrilateral zone faces of the FLAC3D grid. These non-orthogonal connections could cause some errors in pressure calculation,[31,32] although the effect was not taken into consideration in the simulations.

Fig. 3 shows the mesh for the fluid flow analysis. The injection well has a radius of 0.07 m and consists of 24 elements marked in blue. The mesh in the figure is only for the initial state calculation. The mesh geometrical features (volume and connectivity) are continuously updated based on the displacement calculated by FLAC3D through the hydro-mechanical coupling process. In FM1, the central elements denoted by the red indicate the initial fracture zone, which has a hydraulic aperture of 28 μm (creation aperture). The remaining elements represent the closed zone of negligible thickness (10^{-3} μm). The elements for the closed fracture are potential flow paths, but are treated as inactive elements in the fluid flow calculation at the initial stage. Each TOUGH2 element corresponds to a FLAC3D interface element. After shear or tensile failure of an interface element is detected in FLAC3D, the corresponding element is switched to an active element for the subsequent flow calculation in TOUGH2. In FM2, every element initially has a thickness of 10 μm according to the initial hydraulic aperture.

The benchmark calculation assumes that the fluid flow is governed by Darcy's law and the cubic relationship between flow rate and hydraulic aperture.[33] In the present study, the fluid flow within a fault is approximated by two-dimensional horizontal flow within parallel walls separated by a hydraulic aperture and characterized by transmissivity and storativity, which have been primarily used for the flow in well hydraulics in confined aquifers of a finite-thickness.[34] The fault transmissivity, T_f, is proportional to the cube of the hydraulic aperture:

$$T_f = \frac{\rho_f g}{12\mu} b_h^3 \tag{5}$$

where ρ_f is fluid density, g is the gravitational acceleration, μ is fluid dynamic viscosity, and b_h is hydraulic aperture.

Thus, the permeability, k_f, is written as a function of the hydraulic aperture:

$$k_f = \frac{b_h^2}{12} \tag{6}$$

Storativity describes the volume of water released from storage per unit decline in hydraulic head in the aquifer, per unit area of the aquifer. Assuming that a fault is an aquifer with the hydraulic aperture, b_h, and a porosity of 1.0, the fracture storativity can be expressed as follows: [35]

$$S_f = \rho_f g b_h (\alpha_f + \beta) \tag{7}$$

where α_f and β are fault and fluid compressibility, respectively.

The storativity is related to the compressibility of both the fault and the fluid. If we simplify the deformation of the fault as a one-dimensional problem in the normal direction, the fault compressibility can be determined using the fault normal stiffness as follows:

$$\alpha_f = \frac{\Delta b_h / b_h}{\Delta \sigma'_n} = \frac{1}{b_h K_n} \tag{8}$$

Fig. 4 illustrates the data transfer process between TOUGH2 and FLAC3D in the present study. The execution of each program and the data transfer process are repeated at each time step of a TOUGH2 iteration. First, TOUGH2 calculates the pressure of each element and transfers the results to the corresponding interface elements in FLAC3D. Then, the mechanical responses, including fault deformation, are calculated based on an effective stress analysis in which the Biot effective stress coefficient[36] is assumed to be equal to 1.0. The permeability and compressibility of each element are modified according to Eqs. 6 and 8. The geometrical change induced by fault deformation and failure is also updated by rebuilding the mesh for the next calculation in TOUGH2. In this procedure, for each interface element of FLAC3D, a 6-noded prism-shaped element is generated using the updated coordinates of host face and target face. Then, the volume and coordinates of the element, and its connection information, including interface area, nodal distances for the interface, and orientation of the nodal line, are reset for TOUGH2 analysis. Basically, the porosity is calculated by compressibility in TOUGH2, but the value is reset to 1.0 at a beginning of a time step in our simulation because the geometrical change is also updated. The hydraulic aperture is calculated as the distance between the centroids of host face and target face. In FM1, the effect of creation aperture is considered by translating the interface node and its corresponding vertex on the target face by one-half of creation aperture size in opposite directions along the fault normal vector. In the benchmark simulation, the field principal stresses are given by σ_x = 3.3 MPa, σ_y = 6.0 MPa, and σ_z = 7.0 MPa. However, it was observed from the simulation of model FM1 that fracture propagation and fault slip were rarely induced under this stress condition. A few modeling teams of TASK B reported similar findings in the benchmark simulations.[19] To identify the difference between FM1 and FM2 more effectively, we increased the initial shear stress acting on the fault by reducing the intermediate principal stress, σ_y, so that the newly created fracture could reach monitoring points P2 and P3 at 1.5 m from the injection point. Note that we present the results of simulations with the initial stress condition of σ_x = 3.3 MPa, σ_y = 5.3 MPa, and σ_z = 7.0 MPa in the present study. The fracture propagated up to the monitoring points under a lower σ_y of 5.3 MPa in both models. Roller boundaries are set on all six sides of the model and the boundary planes are fixed in the respective normal direction. The initial pressure is set to 0.5 MPa, as estimated from measurements at the site, and the boundary pressure is kept constant during the simulation.

3. Results of benchmark simulations

3.1. Hydrological behavior

This section describes the hydrological behavior of the different fault models, FM1 and FM2, in response to water injection. Figs. 5 and 6 show the profiles of hydraulic aperture and pressure along the fault strike direction (see Fig. 2a) for both fault models. In the figures, the results estimated at 100, 157, 420, 453, and 807 s of water injection are given, which correspond to the ends of injection steps at 1.919, 3.627, 5.484, 6.302, and 3.382 MPa, respectively (see Fig. 1).

The two fault models exhibited completely different evolutions of hydraulic aperture and pressure. In FM1 with an initial 0.5 m radius fracture zone around the injection well, the fluid flowed only through the zone until 420 s. In this phase, the hydraulic aperture increased as a result of elastic deformation with increasing injection pressure and decreasing effective normal stress. Within the fracture zone, a nearly uniform pressure corresponding to the injection pressure developed immediately due to the small fracture volume. The stress conditions in close proximity to the well reached the shear failure criterion, but newly created fracture was not observed until 420 s. Under a higher injection pressure of 6.302 MPa, the shear failure initiated at 421.5 s along the edge of the initial fracture zone, and then propagated rapidly until 453 s to a distance of 1.8 m. As the flow path expanded, the pressure gradient showed transient responses. Under a reduced injection pressure of 3.382 MPa between 453 s and 807 s, the hydraulic aperture decreased through elastic deformation recovery. Note that the creation aperture is irrecoverable in FM1.

In FM2, where the fault was assumed to be initially permeable with hydraulic aperture of 10 μm, the water flowed throughout the entire fault. The hydraulic aperture progressively increased with injection pressure until 453 s by elastic deformation and/or slip-induced dilation, and then decreased by elastic deformation between 453 s and 807 s. Generally, radial fluid flow by injection in a homogeneous, isotropic, confined aquifer exhibits a pressure curve whose gradient decreases with distance from the injection well.[34] The pressure distribution of FM2, however, showed a bell-shaped curve in the early injection steps (157 s in Fig. 6). This might be ascribed to continually and progressively changing fracture hydraulic aperture, permeability and compressibility during the injection. A preliminary study to examine the hydro-mechanical coupling effect suggested that the uncoupled model with the same properties produced the general shape of the pressure curve. In the present coupled model, an increase in hydraulic aperture raised the permeability and reduced the compressibility, resulting in an increase in hydraulic diffusivity. At the early steps, the hydraulic aperture around the well significantly increased in response to water injection, and thus disproportionately high pressure quickly developed in the region. As time proceeded, the injected water pressure transmitted to the boundaries of the model, as shown in the profiles for 420 s and 453 s. It seemed that the chosen extent of the benchmark model domain was not large enough to prevent boundary effects. It is expected that if the boundary condition of constant pressure was not applied, the pressure at the boundaries would increase with time to become higher than 0.5 MPa.

Fig. 7 shows the variations in pressures monitored at points P2 and P3, which are located 1.5 m from the injection point in the fault strike and fault dip directions, respectively (see Fig. 2a). In FM1, the pressures were unchanged at initial pressure of 0.5 MPa until approximately 445 s and then abruptly increased up to 4.2 MPa. Contrary to the nonconsecutive variation in FM1, the pressures in FM2 showed gradual change in response to the injection pressure, even though the pressure began changing at approximately 140 s.

The pressure development correlated closely to the injection flow rate. Fig. 8 shows the variations in injection flow rate for both models. A comparison between the results showed that the FM1 model produced a lower flow rate in the early steps. As mentioned above, the pressure within the initial fracture zone quickly reached steady-state flow because of the small fracture volume. In each injection step, the injection flow rate temporarily reached its peak initially, but decreased to a negligibly small value. With the fracture propagation between 420 and 453 s, the pressure gradient showed transient behavior, and the initial flow rate increased and plateaued during the injection. Newly opened fracture parts raised the differential pressure head between the well and fault, resulting in abrupt changes in the injection flow rate. In the last injection stage with the injection pressure of 3.382 MPa, a back-flow into the well (negative flow rate) was observed in the simulation until the end of injection. The flow rate curve changed slowly compared to those observed in other injection stages, which might be ascribed to the increase in the storativity by irreversible creation aperture. This aspect can also be captured in Fig. 7; after 453 s in FM1, the pressures at the monitoring points were greater than the injection pressure. In FM2, the injection flow rate showed a more stepwise variation in response to injection pressure. FM2 produces higher injection flow rate than FM1 in the earlier steps, because higher differential pressure head gradients developed within a wider range. Shear failure initiated at 215 s and progressively propagated along the fault until 453 s, but the effect of shear failure on the flow rate was not evidently observed contrary to the result of FM1.

3.2. Mechanical behavior

This section describes the mechanical behavior of the FM1 and FM2 models. To assess the mechanical fault behavior, the histories of stress states along the fault were recorded during the simulations, and the shear strength was calculated based on the Coulomb failure criterion using a friction angle of 22º and effective normal stress. Note that if the stress state at the interface node satisfies the Coulomb failure criterion in FLAC3D, sliding is assumed to occur. Then, the magnitude of shear stress is set to the current shear strength with the direction preserved. If the stress state reaches tensile criterion, the fault is assumed to be separated in the normal direction. Actually, a discontinuity in a rock is defined as any significant mechanical break or fracture of negligible tensile strength that already reached failure state.[37] Thus, 'tensile failure' in this study more exactly denotes 'tensile opening' induced by negative effective normal stress.

Generally, in many of the transient subsurface flow problems with respect to fluid injection, it is assumed that total normal stress is constant and the pressure of the injected fluid causes a change in effective normal stress. Assuming that the Biot effective stress coefficient is equal to 1.0, the critical injection pressures above which shear and tensile failure occur, P_{cs} and P_{ct}, can be theoretically derived from the criteria and given conditions for in-situ stress, fault direction, and fault friction angle. The theoretical predictions of P_{cs} and P_{ct} of the benchmark model are found to be 3.99 MPa and 5.60 MPa, respectively. This indicates that shear failure and sliding, prior to tensile opening, is expected to take place at P1.

Fig. 9 shows the variations in injection pressure, total normal stress, effective normal stress, shear stress, and shear strength monitored at injection point P1. The effective normal stress and shear strength showed a degradation or increase in response to change in injection pressure in the simulations. The stress state at P1 reached the shear failure condition when imposing an injection pressure much higher than the expectation; shear failure at P1 occurred at 5.484 MPa in FM1, and 4.511 MPa in FM2. Tensile fracture opening due to negative normal stress was not observed in either model. Contrary to the theoretical assumption, total normal stress acting on the fault did not remain constant but increased in the simulations, and therefore the effective normal stress and shear strength of the model were higher than the calculation. This aspect might be ascribed to the physical constraint of normal displacement and is more evident in FM1 than in FM2. In FM1, where the initial rupture zone was only allowed to deform in the normal direction, compressive stress was concentrated along the edge, which raised the total normal stress. After the additional fracture was created, total normal stress was reduced. The increase in total normal stress until approximately 150 s observed in FM2 can be explained in the same way.

Fig. 10 shows the fault shear displacement and failure zone, which were estimated at 453 s. In the displacement contour, the red denotes the maximum value and the blue denotes zero. Fig. 11 shows the variations in normal and shear displacements monitored at P1 and P2. In both models, the fault shear displacement occurred in the dip direction after shear failure and displacement in the strike direction was negligible. As mentioned, an increase in total normal stress shifted the point of the onset of shear failure to higher injection pressure, which caused FM2 to have a greater shear displacement and larger failure zone.

Fig. 12 shows the displacement contours of the surrounding host rock estimated at 420, 453, and 807 seconds of injection. Fig. 13 shows the relative displacement of the upper anchor to lower anchor. The rock deformation was limited to small regions adjacent to the newly fractured zone in FM1, whereas a large deformation was predicted along the entire fault in FM2. It is found from the anchor displacement in Fig. 13 and the displacements at injection point P1 in Fig. 11a that the anchor displacement is primarily correlated with the fault displacement. The anchor displacement was oriented in the fault normal direction before shear failure, and then inclined towards the dip direction after shear failure. The decreases in dy and dz between 420 and 453 s indicate that the upper surface of the hanging wall moved downward relative to the lower surface of footwall due to fault slip. This is also evident from the observations of rock and fault displacements in Fig. 12.

4. Application of developed model to fault slip experiment at Mont Terri Rock Laboratory

4.1 Descriptions of minor fault reactivation experiment

The Mont Terri Rock Laboratory is an underground research facility located at a depth of 280 m below the surface in Saint Ursanne in the canton of Jura. The research facility can be accessed through the security gallery of the Mont Terri tunnel (Fig. 14). In the facility, various experiments have been conducted to investigate and analyze the hydrogeological, geochemical, and rock mechanical characteristics of argillaceous formations, specifically the Opalinus Clay layer, which has been considered as the preferred host rock for high-level waste disposal in Switzerland.[38]

The Mont Terri rock laboratory is intersected by a major fault called the 'Main Fault'. The fault core is 0.8 – 3.0 m thick and is bounded by two major fault planes oriented 156°/45° (dip direction/dip angle) and 165°/40°, respectively. Several fault planes were observed and they were almost parallel to bedding planes oriented 145 – 155°/ 50 – 55°. The dip directions and dip angles of the fault planes ranged from 120° to 150° and from 50° to 70°, respectively.

A series of fault reactivation experiments were conducted in the major and minor planes of the Main Fault, which were aimed at quantifying hydraulic and mechanical characteristics of those major and minor fault planes in response to water injection. Fig. 15 shows the locations and apparatus of the fault reactivation experiments.[39, 40] The fault reactivation experiments were conducted at four borehole interval sections (at depths of 47.2 m of borehole BFS1 and 44.65, 40.6, and 37.2 m of BFS2). In each test, a fault plane was stimulated by pressure-controlled water injection and the flow rate, pressure, displacement variations, and induced seismicity were monitored in the injection and monitoring boreholes. More detailed descriptions of the experiments are given by Gulglielmi et al.[39]

The experiment for the numerical simulation of Step 2 of Task B corresponds to the injection test conducted at 37.2 m of BFS2. This section is the farthest from the fault core and the host rock is nearly intact rock affected by a few polished and striated secondary faults. The injection test was conducted for approximately 9,500 s. The initial period of 807 s was taken for the numerical simulation.

Fig. 16 shows the field experimental results. Fig. 16a shows the injection chamber pressure and injection flow rate measured at 37.2 m of borehole BFS2 and the pressure monitored at a packed-off interval in borehole BFS4. The monitoring point is located at a distance of approximately 1.5 m in the fault strike direction. Fig. 16b shows the vertical, northern, and western components of the relative displacement of upper anchor to lower anchor, which are initially spaced at a vertical distance of 0.5 m and installed in the hanging wall and footwall.

The pressure response at the monitoring point can be characterized by its abrupt increase occurring after 420 s of injection, which indicates the onset of fracture opening at the monitoring point. The consistent injection flow rate between 420 and 453 s reveals the increase in hydraulic conducting aperture followed by fracture propagation along the fault plane. The relative displacement of upper anchor to lower anchor initially corresponds to a normal closure of the fault, and then changes with injection pressure.

4.2 Simulation of the experimental results

The simulation of Step 2 is aimed at interpretively simulating the field experimental results by selecting appropriate boundary and initial conditions, constitutive models, and properties for the rock and fault. The modeling approach described in Section 2, including assumptions and constitutive laws, was taken for the simulation. We adopted the model FM1 to consider the hydraulic aperture evolution. The comparisons between field data in Fig. 16 and the results of benchmark simulations in Figs. 7, 8, and

13 reveal that FM1 can more reasonably capture the characteristics of the pressure build-up at the monitoring point and the variation in injection flow rate observed in the site than FM2. In FM2, the fault is assumed to be an open and permeable flow path regardless of fracture failure. Consequently, the immediate effect of fracture opening on the change in the injection flow rate cannot be properly simulated, even though the pressure build-up at monitoring points would be controlled by assigning a smaller initial aperture.

According to Martin and Lanyon[41] and Yong et al.[42], the Mont Terri rock laboratory is subjected to an in-situ stress state where the maximum principal stress, σ_1 = 6 – 7 MPa, the intermediate principal stress, σ_2 = 4 – 5 MPa, and the minimum principal stress, σ_3 = 0.6 – 3 MPa. The average orientations (trend/plunge) are analyzed to be 210º/70º, 320º/10º, and 50º/20º, respectively. Based on the studies, we assume that σ_1 corresponds to the vertical principal stress σ_v, and σ_2 and σ_3 to the two horizontal principal stresses, σ_H and σ_h, which are oriented at 320º and 50º in the model. For simplicity of assigning the boundary and initial stress conditions to the model, we made the axes of coordinate, *x*, *y,* and *z*, parallel to directions of σ_h, σ_H, and σ_v, respectively, by rotating the geometric information of fault and in-situ stresses.

Fig. 17 shows an example of a FLAC3D model rotated with respect to the *z* axis by 40º. As in the benchmark calculation, the boundaries were assigned a constant pressure in fluid flow analysis, and the grid points were fixed in the out-of-plane direction in mechanical analysis. The initial fluid pressure was set to 0.5 MPa, as estimated from measurements at the site.

A series of simulations were performed under various conditions to examine the effects of influencing factors and to reproduce the field data shown in Fig. 16. Table 2 lists the ranges of the input parameters for fault and in-situ stress. The values chosen in the simulations showing the best match (Case 1) and second-best match (Case 2) are also given in the table. The friction angle, dilation angle, and tensile strength of the fault were fixed in the calibration. The input parameters of the host rock and fluid are the same as those used for benchmark simulations (see Table 1).

With the priority given to the following characteristics observed from the field data, we calibrated the numerical model by improving the parameter set in a trial-and-error manner until the responses of the numerical model matched the field data.

1) Flow rate and volume of injected water between 420 and 453 s
2) Abrupt change in pressure at monitoring point after 420 s
3) Magnitude and direction of anchor displacement vector

The numerical and experimental results of injection flow rate and pressure at the monitoring point are compared in Figs. 18 and 19. The numerical results were obtained from the simulation case showing the best match. Note that little attempt was made for reproducing the variation in injection flow rate within the first 420 s during which the fracture failure was not expected to occur. The erratic variation observed in the field data in the duration is beyond the scope of the present study. In terms of the injection flow rate and injected water volume between 420 and 453 s, the numerical model showed good agreement with the experimental results. In the model, the injection flow rate showed an instantaneous rise to a peak followed by a quick drop to zero in each injection step before 430 s. Then, it increased up to 21 liter/min that was consistently maintained until 453 s.

Fig. 20 shows the pressure contours estimated at 425, 430, and 453 seconds. In the figure, r is the radius of the created fracture zone at each moment. As seen in the figure, small regions around the initial fracture zone only functioned as flow paths in the early stage, and therefore high pressure quickly developed within the zone. As new fracture areas were created through rupture propagation, the pressure developed in a transient manner, which resulted in continuous increases in the injection flow rate. The stress state at the monitoring point reached the failure criteria at approximately 430 s, and then the pressure started to increase. Even though the pressure curve obtained from numerical model exhibited a higher peak and slower responses than field observations, it reasonably reproduced the overall tendency, including timing of the increase. The volume of injected water between 420 and 453 s was calculated to be 8.0×10^{-3} m^3 in the numerical model, which corresponds well to 7.7×10^{-3} m^3 that is calculated from the curve of the field data. After 453 s, when a lower injection pressure of 3.382 MPa was imposed, negative flow rate values were estimated, which indicated flow-back into the well due to injection pressure being lower than the fault pressure. In the field, some flow-back was observed at the very end of the test even though it was not measured.

The numerical and experimental results for variations in relative displacement between two anchors are compared in Fig. 21. They are within reasonable agreement, even though the numerical model estimated 3 – 4 times larger vertical components than the field data. In the numerical model, the upper anchor moved upward and in a southeastern direction horizontally, while the lower one was displaced in the exact opposite direction. If we decompose the relative displacement vector into two components in fault shear and normal directions, it is evidently observed that the anchor displacements are reflective of the fault movement. In Fig. 22, the components of the relative displacement vector in fault normal and shear directions, d_n and d_s, are presented and compared to normal and shear displacements, u_n and u_s, of injection point P1. The anchor movement was primarily affected by the elastic normal expansion of the fault before 420 s, and then dominated by fault slip after 420 s. The upper anchor slid along the fault, which resulted in a decrease in the vertical component between 420 and 453 s. With increasing fault shear displacement, the magnitudes of the horizontal components increased as shown in Fig. 21. After 453 s, the displacement in every direction was recovered due to elastic recovery in the fault normal direction.

4.3 Discussion

In the calibration procedure, it was found that the hydro-mechanical responses of the fault to injection were not only interrelated but also affected by input parameters in conflicting ways. The complicated effects of several input parameters made it difficult to find a parameter set that satisfactorily reproduced all the experimental data in Fig. 16. We placed more emphasis on producing a reliable representation of the characteristics regarding the fracture opening and propagation, and thus focused on the variations in injection flow rate and pressure response. As a result, the anchor displacement curve even in the best matching case was in relatively poor agreement with field data.

The injection flow rate and the pressure at the monitoring point were mainly dependent on the fracture opening and propagation process. In other words, the onset and extent of the failure can be controlled by adjusting the in-situ stress direction and magnitude, fault direction, and strength parameters. According to the theory of stresses in three dimensions[43], we can calculate the normal stress, σ_n, and shear stress, τ, on a fault plane whose normal vector in the principal coordinate system is $n = (n_1, n_2, n_3)$, as Eqs. 9 and 10.

$$\sigma_n = \sigma_1 n_1^2 + \sigma_2 n_2^2 + \sigma_3 n_3^2 \tag{9}$$

$$\tau^2 = (\sigma_1 - \sigma_2)^2 n_1^2 n_2^2 + (\sigma_2 - \sigma_3)^2 n_2^2 n_3^2 + (\sigma_3 - \sigma_1)^2 n_3^2 n_1^2 \tag{10}$$

Using the stresses and fault strength properties, theoretical estimates of the critical pressures above which shear and tensile failures of fault occur, P_{cs} and P_{ct}, can be calculated based on the failure criteria. In the calibration process, we repeatedly adjusted the influencing input parameters in a trial-and-error manner so that the shear or tensile failure along the fault could be induced between 420 and 453 s. The initial condition of stresses on the fault plane and cohesion were the dominant parameters determining the onset and extent of the failure. Small normal stress and/or large shear stress and/or small cohesion promoted the fault failures, and vice versa.

In the best matching case, the cohesion of interface elements was set to zero, and thus shear failure was theoretically expected to occur prior to tensile failure: the calculated values of P_{cs} and P_{ct} were 4.93 MPa and 5.01 MPa. However, in the simulation, both shear and tensile failures initiated at 422 s within the regions around the injection well. The fault effective normal stress dropped to a negative value instantaneously due to the imposed injection pressure, and the stress condition simultaneously satisfied the shear and tensile failure criteria. New fractures were created at 424 s and propagated to the monitoring points by approximately 430 s. The injection flow rate after failure was primarily influenced by elastic and plastic aperture enhancements. Therefore, the injection flow rate evidently increased with decreasing normal stiffness and increasing creation aperture size.

The anchor displacement in the elastic stage was influenced by the normal stiffness and fault direction. The magnitude decreased with increasing normal stiffness, and the direction exactly corresponded to the normal direction of the fault. The effects were evident in the numerical model, and thus it was possible to better match the field data by adjusting the influencing parameters. However, choices of the parameters were limited, because they also affected the elastic hydraulic aperture and the onset of fracture failure, resulting in different injection flow rate and pressure response.

After the occurrence of fracture failure, the anchor displacement was dominated by fault shear and normal displacements. In particular, the fault shear displacement controlled the vertical component of the relative displacement between the anchors. With a large shear displacement, the vertical component fell below zero, which means that upper anchor moved downward relative to the lower anchor due to fault slip. In other words, for a more reasonable representation of anchor displacement curves, the shear displacement should be limited. In our model, the most influential factor on the shear displacement was the initial shear stress acting along a fault. We attempted to minimize the initial shear stress by adjusting the principal stresses in a range of 6.0 – 7.0, which was given in the literature[41, 42], but even the simulation with the smallest minimum initial shear stress exhibited a large shear displacement.

Figs. 23, 24, and 25 show the comparisons between the numerical results of Case 2 and field experimental results for injection flow rate, pressure at monitoring point, and relative displacement of the upper anchor to lower anchor. In terms of the injection flow rate and pressure response, Case 2 under the maximum principal stress of 7.0 MPa showed better agreement with field data than Case 1. However, the fault reactivation produced shear displacement of hundreds of micrometers, and consequently anchor displacement at the site was poorly represented. In Case 1, which showed the best match, the maximum principal stress was chosen as 5.1 MPa so that the fault could have a minor value of the initial shear stress, 0.032 MPa. As shown in Figs. 21 and 22, the fault slip was small, and the vertical anchor movement was more reasonably reproduced. From these findings, it can be inferred that the hydraulic aperture at the site was associated with tensile opening rather than hydro-shearing. Guglielmi et al.[39] indicated that the in-situ stress condition of the research site might be different from that reported by Martin and Lanyon[41] and Yong et al.[42] because of the excavation followed by stress redistribution. The simple assumption for vertical and horizontal principal directions taken in this study might also impede the calibration.

Although the emphasis is placed on representing the hydro-mechanical responses associated with fault reactivation in the present study, the proposed model can be used for the prediction of induced seismicity. For example, the seismic moment can be estimated from the simulation results of the fault shear displacement and failure zone shown in Fig. 26. Based on the rock mass shear modulus, average slip (the area-weighted average of shear displacements over failed interface elements) and slip area, a seismic moment, M_o, of 1.57×10^5 Nm is predicted. The relation between seismic moment and magnitude reported by Hanks and Karnamori[44] gives a moment magnitude, M_w, of -2.6. Since we used a simple elastic-perfectly plastic model for the fault frictional process, the estimate of seismic moment may be inaccurate. With the appropriate selection of the properties and behavior models based on laboratory and field experiments, a better accuracy can be achieved in a further study.

5. Summary and conclusions

In the present study, we have numerically simulated the water injection into a fault and examined the coupled hydro-mechanical processes along the fault and the surrounding rock. We proposed a modeling approach using the TOUGH-FLAC simulator through benchmark calculations for well-defined models, and demonstrated its applicability by reproducing field experiment results obtained at the Mont Terri Rock Laboratory in Switzerland.

In our model, elements of aperture-sized thickness are used for the fluid flow analysis in TOUGH2, whereas interface elements of zero-thickness are used for the mechanical calculation in FLAC3D. In the coupling process, the geometrical features, hydrological properties, and effective stress are continuously updated by the sequential executions of both codes and the data transfer between the elements and interface elements. This modeling approach allowed the explicit representation of the fault, preventing the involvement of many parameters and assumptions for equivalent thickness and fault properties. Moreover, the merit of the interface element enabled us to observe how the tensile opening and hydro-shearing played roles in hydraulic aperture in a direct manner. The transient responses of the fault, including pressure response, injection flow rate, elastic behavior, fracture failure, and stepwise pressurization were analyzed for two different fault models, FM1 and FM2. The two fault models exhibited entirely different behaviors due to different pathway evolutions and the consequent pressure build-up, which indicates the importance of appropriate descriptions of hydraulic aperture in fault modeling.

The developed model was applied to the fault reactivation experiment conducted at the ‘Main Fault’ intersecting the low permeability clay formation of the Mont Terri Rock Laboratory in Switzerland. We used the model FM1 to reproduce the fracture opening and propagation processes and the hydro-mechanical characteristics observed at the site. With priority given to the reliable representation of fracture failure, the numerical model was calibrated to the field data by adjusting the input parameters in a trial-and-error manner. In this procedure, the effects of input parameters such as dip angle, dip direction, shear and normal stiffnesses, cohesion, fault creation aperture size, and in-situ stress conditions were discussed. In the best matching simulation, the results of flow rate and pressure build-up at high injection pressure were in good agreement with the field experimental results. The relative displacement of anchors installed in proximity to the injection point showed a discrepancy between the numerical and experimental results. Even though the vertical displacement was $3-4$ times greater than the experimental result, a fair agreement was obtained in the horizontal displacement and the overall variation tendency.

It was found from the benchmark calculations and the simulation of field reactivation experiment that the proposed model can capture the process of fracture opening and propagation, and thus provide a reasonable prediction of the hydro-mechanical behavior associated with fault reactivation by fluid injection. It is expected that this modeling approach can be applied to various fault hydraulic models tailored to suit field observations. However, to ensure the applicability of the modeling approach to field-scale problems there are a few technical problems that should be addressed in further study. In particular, special attention should be paid when handling the interface elements and their contacts.[22] For example, the use of nonplanar interfaces, overlapping interfaces, and multiple intersecting interfaces may cause some problems in detecting appropriate contacts and thus in calculating forces and displacements. The numerical model will be enhanced by continuing collaboration and interaction with other research teams of DECOLVAEX-2019 Task B and validated using available field data in further studies.

Acknowledgments

The authors appreciate and thank the DECOVALEX-2019 Funding Organizations Andra, BGR/UFZ, CNSC, US DOE, ENSI, JAEA, IRSN, KAERI, RWM, SÚRAO, SSM, and Taipower for their financial and technical support of the work described in this paper. The statements made in the study are, however, solely those of the authors and do not necessarily reflect those of the Funding Organizations. This research was also supported by the Basic Research Project of the Korea Institute of Geoscience and Mineral Resources (KIGAM, GP2020-010) funded by the Ministry of Science and ICT, Korea. LBNL's funding was provided by the Spent Fuel and Waste Science and Technology, Office of Nuclear Energy, of the U.S. Department of Energy under Contract Number DE-AC02-05CH11231 with Lawrence Berkeley National Laboratory.

References

1. Bohloli B, Choi JC, Skurtveit E, Grande L, Park J, Vannest M. Criteria of fault geomechanical stability during a pressure build-up. 2015 IEAGHG report 2015/04. Cheltenham; 2015.
2. Wiprut DJ, Zoback MD. Fault reactivation, leakage potential, and hydrocarbon column heights in the northern North Sea. In: Hydrocarbon Seal Quantification. Norwegian Petroleum Society Special Publication. 2002; 11: 203–219.
3. Vidal-Gilbert S, Tenthorey E, Dewhurst D, Ennis-King J, Van Ruth P, Hillis R. Geomechanical analysis of the Naylor Field, Otway Basin, Australia: implications for CO2 injection and storage. International Journal of Greenhouse Gas Control. 2010; 4: 827–839.
4. Rinaldi AP, Rutqvist J, Cappa F. Geomechanical effects on CO2 leakage through fault zones during large-scale underground injection. International Journal of Greenhouse Gas Control. 2014; 20: 117–131.

5. Rutqvist J, Dobson PF, Garcia J, Hartline C, Jeanne P, Oldenburg CM, Vasco DW, Walters M. The northwest Geysers EGS demonstration project, California: Pre-stimulation modeling and interpretation of the stimulation. Mathematical Geosciences. 2015; 47: 3–29.
6. Nguyen TS, Guglielmi Y, Graupner B, Rutqvist J. Mathematical modelling of fault reactivation induced by water injection. Minerals. 2019; 9: 282.
7. Rinaldi AP, Rutqvist J. Joint opening or hydroshearing? Analyzing a fracture zone stimulation at Fenton Hill. Geothermics. 2019; 77: 83–98.
8. Vidal-Gilbert S, Nauroy JF, Brosse E. 3D geomechanical modelling for CO2 geologic storage in the Dogger carbonates of the Paris Basin. International Journal of Greenhouse Gas Control. 2009; 3: 288–299.
9. Cuisiat F, Jostad HP, Andresen L, Skurtveit E, Skomedal E, Hettema M, Lyslo K. Geomechanical integrity of sealing faults during depressurization of the Statfjord field. Journal of Structural Geology. 2010; 32: 1754–1767.
10. Cappa F, Rutqvist J. Modeling of coupled deformation and permeability evolution during fault reactivation induced by deep underground injection of CO2. International Journal of Greenhouse Gas Control. 2011; 5: 336–346.
11. Morris JP, Hao Y, Foxall W, McNab W. A study of injection-induced mechanical deformation at the In Salah CO2 storage project. International Journal of Greenhouse Gas Control. 2011; 5:270–280.
12. Orlic B, Heege J, Wassing B. Assessing the integrity of fault- and top seals at CO2 storage sites. Energy Procedia. 2011; 4: 4798–4805.
13. Pirayehgar A, Dusseault MB. 2015, Numerical investigation of seismic events associated with hydraulic fracturing. In: Proceedings of 13th ISRM International Symposium. Montreal, Canada. 2015: ISRM-13CONGRESS-2015-168.
14. Zangeneh N, Eberhardt E, Bustin RM. Investigation of the influence of natural fractures and in-situ stress on hydraulic fracture propagation using a distinct-element approach. Canadian Geotechnical Journal. 2015; 52: 926–946.
15. Amini A, Eberhard E. Influence of tectonic stress regime on the magnitude distribution of induced seismicity events related to hydraulic fracturing. Journal of Petroleum Science and Engineering. 2019; 182: 106284.
16. Leijon B. Mechanical properties of fracture zones. SKB Technical Report TR 93-19; 1993.
17. Rutqvist J, Wu YS, Tsang CF, Bodvarsson G. A modeling approach for analysis of coupled multiphase fluid flow, heat transfer, and deformation in fractured porous rock. International Journal of Rock Mechanics and Mining Sciences. 2002; 39: 429–442.
18. Birkholzer JT, Tsang CF, Bond AE, Hudson JA, Jing L, Stephansson O. 25 years of DECOVALEX - Scientific advances and lessons learned from an international research

collaboration in coupled subsurface processes. International Journal of Rock Mechanics and Mining Sciences. 2019; 122: 103995.

19. Rutqvist J, Graupner B, Guglielmi Y, Birkholzer J, Kim T, Maßmann J, Nguyen TS, Park JW, Shiu W, Urpi L, Yoon JS, Ziefle G. An international simulation study of a controlled fault activation experiment at Mont Terri Laboratory. International Journal of Rock Mechanics and Mining Sciences. (this issue, to be submitted)
20. Guglielmi Y, Elsworth D, Cappa F, Henry P, Gout C, Dick P, Durand J. In situ observations on the coupling between hydraulic diffusivity and displacements during fault reactivation in shales. Journal of Geophysical Research: Solid Earth. 2015; 120: 7729–7748.
21. Pruess K, Oldenburg C, Moridis G. TOUGH2 User's guide, ver. 2.0. Lawrence Berkeley National Laboratory (LBNL) Report LBL-43134. Berkeley: LBNL; 1999.
22. Itasca Consulting Group Inc. FLAC3D manual: Fast Lagrangian analysis of continua in 3 dimensions – ver. 5.0 manual. Minnesota: Itasca Consulting Group Inc; 2012.
23. Tsang CF, Birkholzer J, Rutqvist J. A comparative review of hydrologic issues involved in geologic storage of CO2 and injection disposal of liquid waste. Environmental Geology. 2008; 54: 1723–1737.
24. Cappa F, Rutqvist J. Seismic rupture and ground accelerations induced by CO2 injection in the shallow crust. Geophysical Journal International. 2012; 190: 1784–1789.
25. Kim HM, Rutqvist J, Ryu DW, Choi BH, Sunwoo C, Song WK. 2012. Exploring the concept of compressed air energy storage (CAES) in lined rock caverns at shallow depth: A modeling study of air tightness and energy balance. Applied Energy. 2012; 92: 653–667.
26. Rutqvist J. Status of the TOUGH-FLAC simulator and recent applications related to coupled fluid flow and crustal deformations. Computers & Geosciences. 2012; 37: 739–750.
27. Rutqvist J, Dobson PF, Garcia J, Hartline C, Jeanne P, Oldenburg CM, Vasco DW, Walters M. The northwest Geysers EGS demonstration project, California: Pre-stimulation modeling and interpretation of the stimulation. Mathematical Geosciences. 2015; 47: 3–29.
28. Park JW, Rutqvist J, Ryu DW, Park ES, Synn JH. Coupled thermal-hydrological-mechanical behavior of rock mass surrounding a high-temperature thermal energy storage cavern at shallow depth. International Journal of Rock Mechanics & Mining Sciences. 2016; 83: 149–161.
29. Zbinden D, Rinaldi AP, Urpi L, Wiemer S. On the physics-based processes behind production-induced seismicity in natural gas fields. Journal of Geophysical Research: Solid Earth. 2017; 122: 3792–3812.
30. Urpi L, Rinaldi AP, Rutqvist J, Wiemer S. Fault stability perturbation by thermal pressurization and stress transfer around a deep geological repository in a clay formation. Journal of Geophysical Research: Solid Earth. 2019; 124: 8506–8518.
31. Croucher AE, O'Sullivan MJ. Approaches to local grid refinement in TOUGH2 models. In:

Proceedings of 35th New Zealand Geothermal Workshop, Rotorua, New Zealand. 2013: 17–20.

32. Bonduà S, Battistelli A, Berry P, Bortolotti V, Consonni A, Cormio C, Geloni C, Vasini EM. 3D Voronoi grid dedicated software for modeling gas migration in deep layered sedimentary formations with TOUGH2-TMGAS. Computers & Geosciences. 2017; 108: 50–55.
33. Witherspoon PA, Wang JSY, Iwai K, Gale JE. Validity of Cubic Law for Fluid Flow in a Deformable Rock Fracture. Water Resources Research. 1980; 16: 1016–1024.
34. Freeze RA, Cherry JA. Groundwater. New Jersey: Prentice-Hall; 1979.
35. Rutqvist J, Tsang CF, Stephansson O. Determination of fracture storativity in hard rocks using high pressure testing. Water Resources Research. 1998; 34: 2551–2560.
36. Biot MA, Willis DG. The elastic coefficients of the theory of consolidation. Journal of Applied Mechanics. 1957; 24: 594–601.
37. Priest SD. Discontinuity analysis for rock engineering. New York: Chapman & Hall; 1993.
38. Bossart P, Bernier F, Birkholzer J, Bruggeman C, Connolly P, Dewonck S, Fukaya M, Herfort M, Jensen M, Matray JM, Mayor JC, Moeri A, Oyama T, Schuster K, Shigeta N, Vietor T, Wieczorek K. Mont Terri Rock Laboratory, 20 years of research: Introduction, site characteristics and overview of experiments. Swiss Journal of Geosciences. 2017; 110: 3–22.
39. Guglielmi Y, Birkholzer J, Rutqvist J, Jeanne P, Nussbaum C. Can fault leakage occur before or without reactivation? Results from an in situ fault reactivation experiment at Mont Terri. Energy Procedia. 2017; 114: 3167–3174.
40. Guglielmi Y, Cappa F, Lancon H, Janowczyk J, Rutqvist J, Tsang CF, Wang JSY. ISRM suggested method for step-rate injection method for fracture in-situ properties (SIMFIP): Using a 3-components borehole deformation sensor. Rock Mechanics and Rock Engineering. 2017; 47: 303–311.
41. Martin CD, Lanyon GW. Measurement of in-situ stress in weak rocks at Mont Terri Rock Laboratory, Switzerland. International Journal of Rock Mechanics & Mining Sciences. 2003; 40: 1077–1088.
42. Yong S, Kaiser PK, Loew S. Influence of tectonic shears on tunnel-induced fracturing. International Journal of Rock Mechanics & Mining Sciences. 2010; 47: 894–907.
43. Jaeger JC, Cook NGW, Zimmerman RW. Fundamentals in rock mechanics. 4th edition. Oxford: Blackwell publishing; 2007.
44. Hanks TC, Kanamori H. A moment magnitude scale. Journal of Geophysical Research: Solid Earth. 1979; 84: 2348–2350.

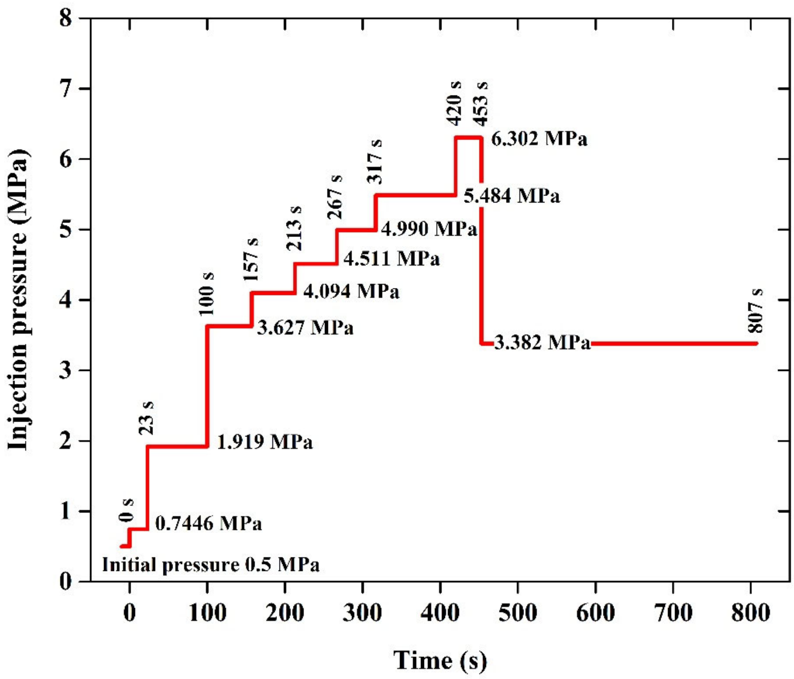

Fig. 1. Stepwise pressure injection scheme for benchmark calculations.

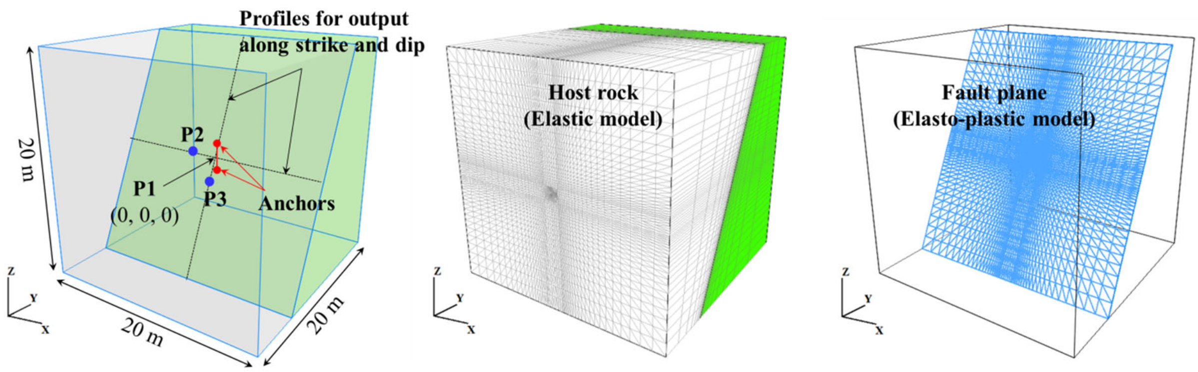

(a) (b) (c)

Fig. 2. Model domain and numerical mesh in FLAC3D for benchmark calculations: (a) model geometry and monitoring point locations, (b) host rock zone elements, and (c) fault interface elements.

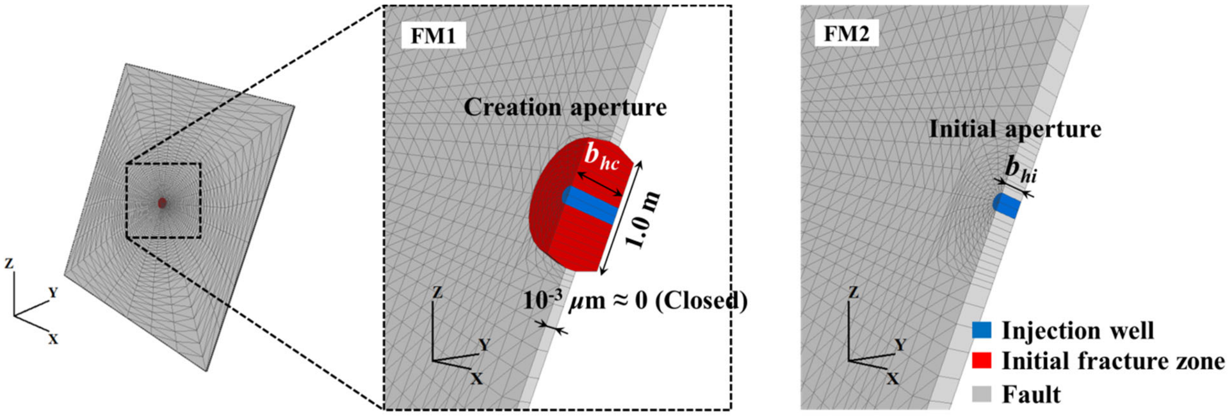

Fig. 3. Initial mesh for fluid flow analysis in TOUGH2.

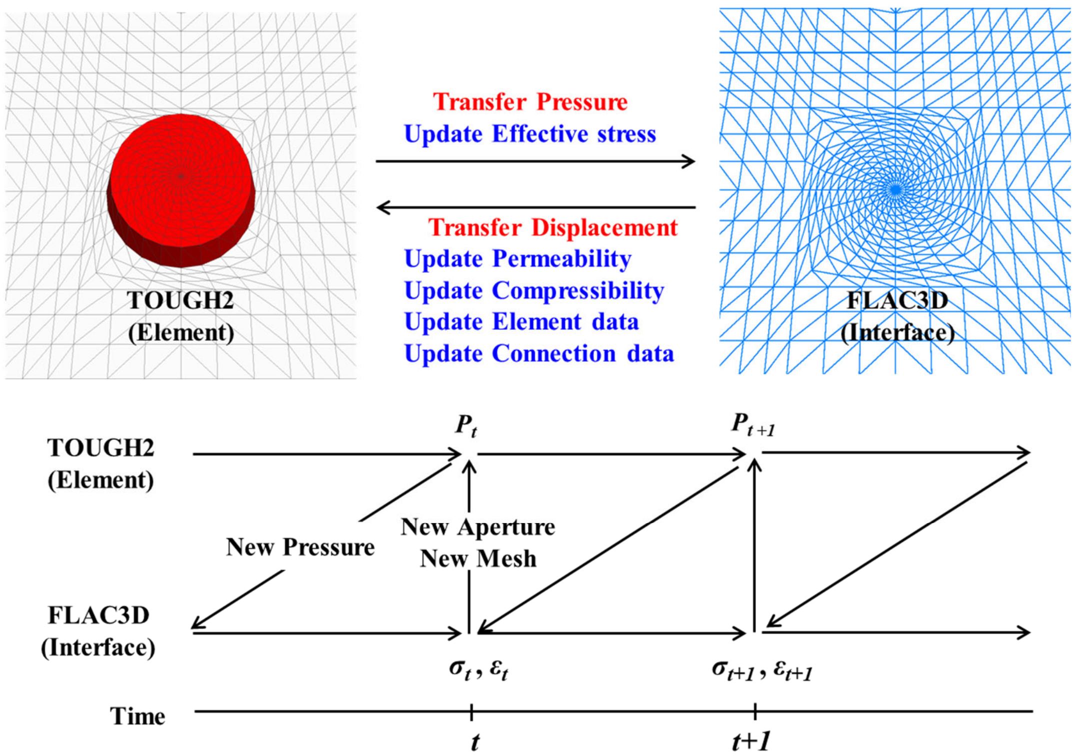

Fig. 4. Hydro-mechanical coupling process and data transfer between volume elements of TOUGH2 and interface elements of FLAC3D.

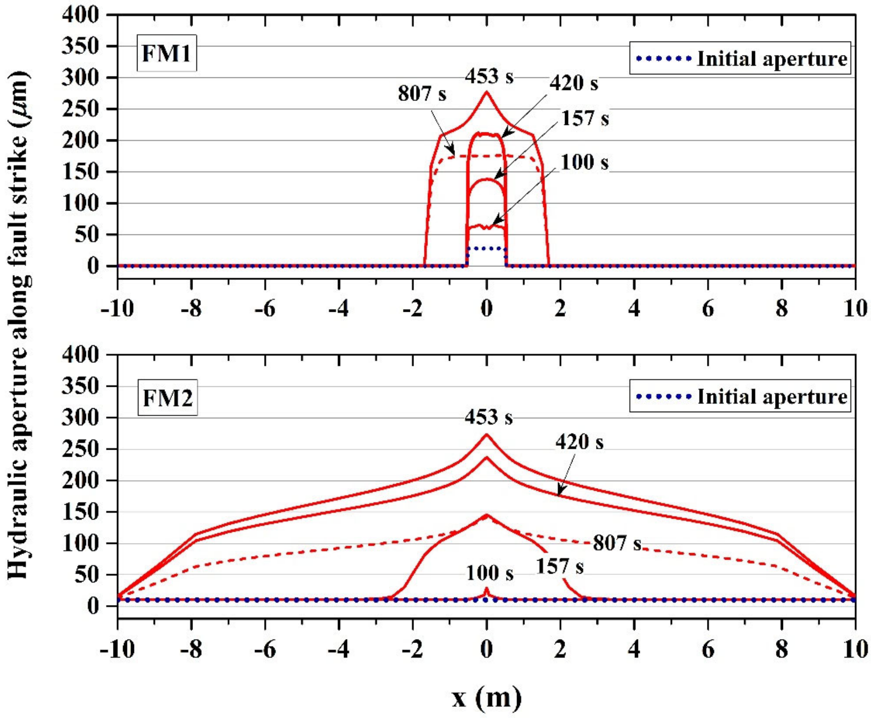

Fig. 5. Profiles of hydraulic aperture along the fault strike estimated at 100, 157, 420, 453, and 807 s of water injection.

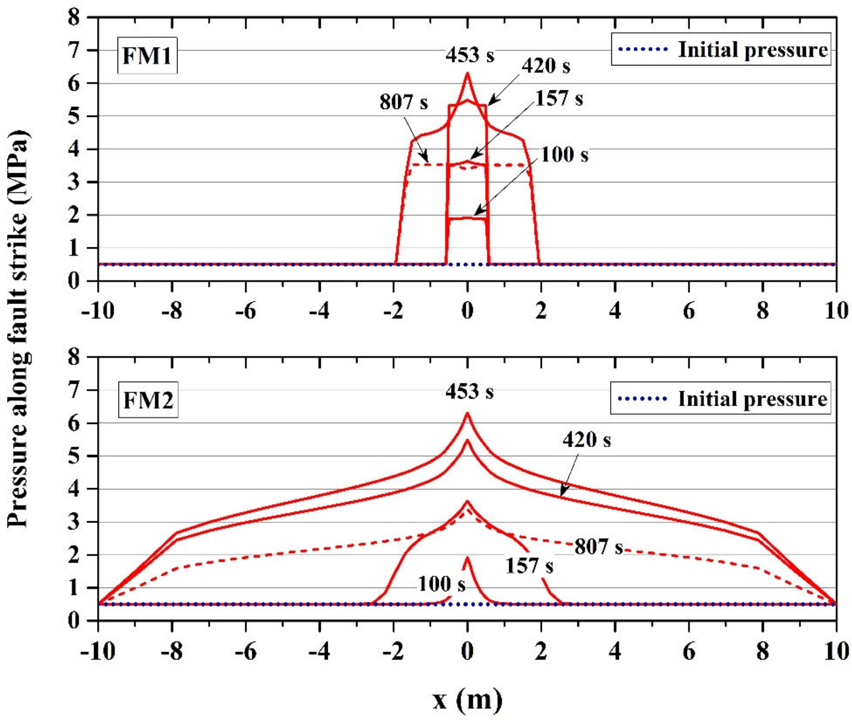

Fig. 6. Profiles of pressure along the fault strike estimated at 100, 157, 420, 453, and 807 s of water injection.

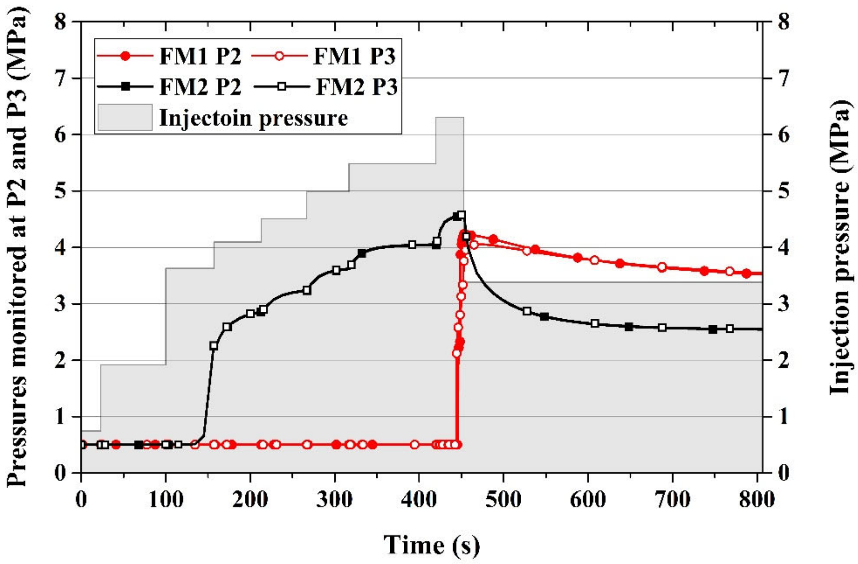

Fig. 7. Variations in pressures monitored at P2 and P3; the red lines denote the results of FM1 and the black lines denote the results of FM2.

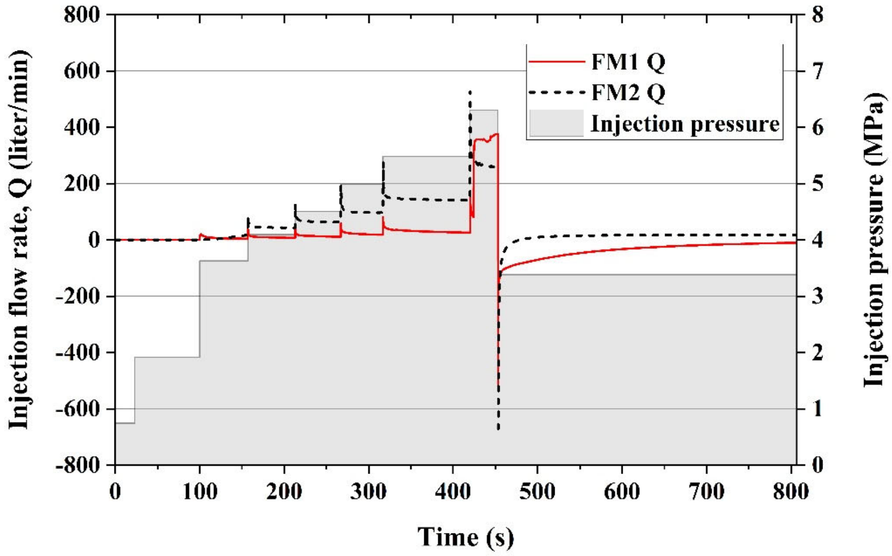

Fig. 8. Variations in injection flow rate at P1; the red denotes the result of FM1 and the black denotes the result of FM2.

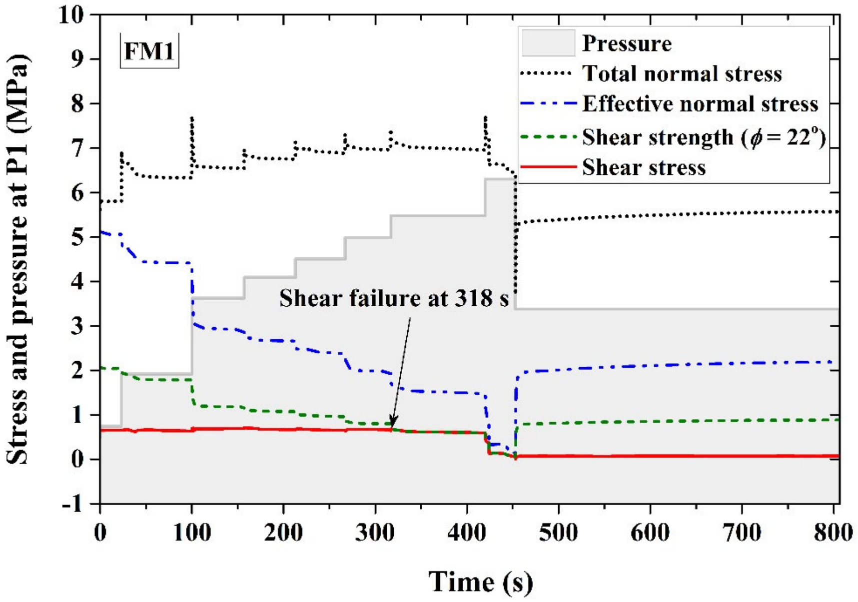

(a)

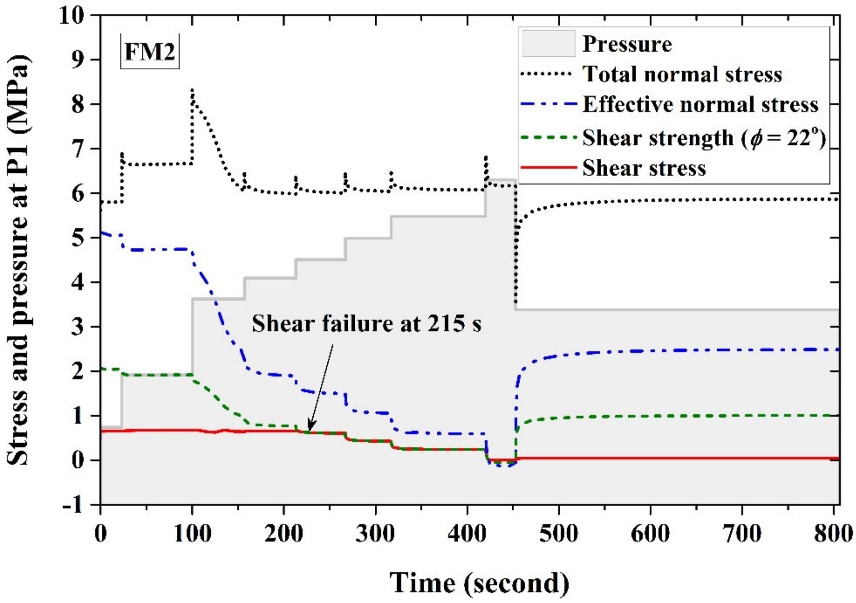

(b)

Fig. 9. Variations in pressure, total normal stress, effective normal stress, shear stress and shear strength monitored at injection point P1: (a) FM1 and (b) FM2.

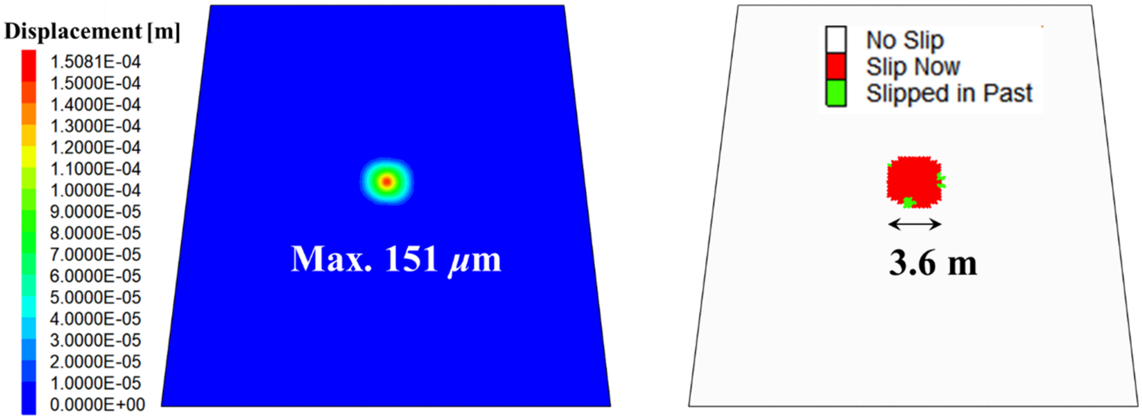

(a)

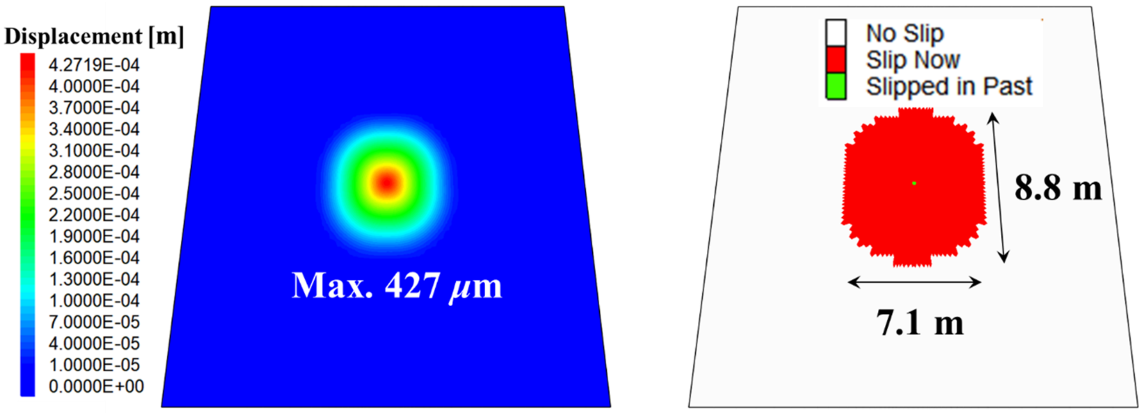

(b)

Fig. 10. Shear displacement and extent of shear failure zone estimated at 453 s of water injection with injection pressure of 6.302 MPa: (a) FM1 and (b) FM2.

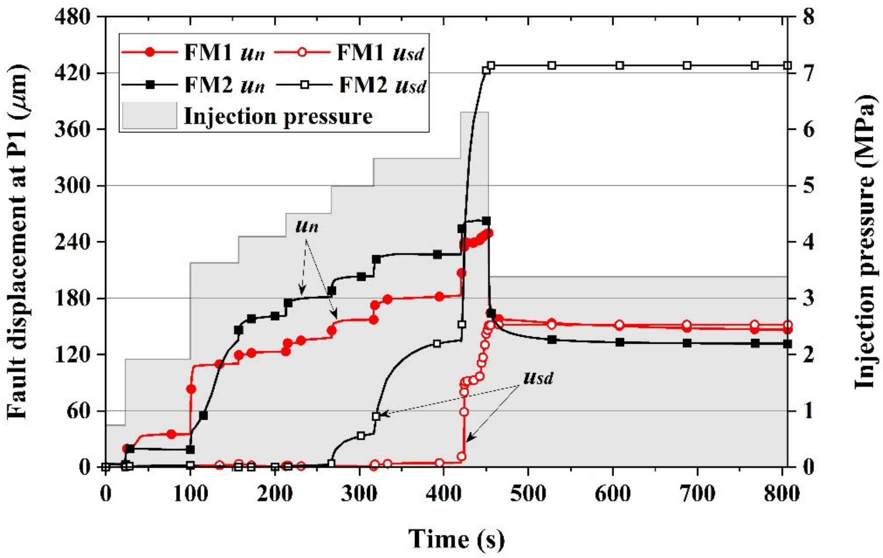

(a)

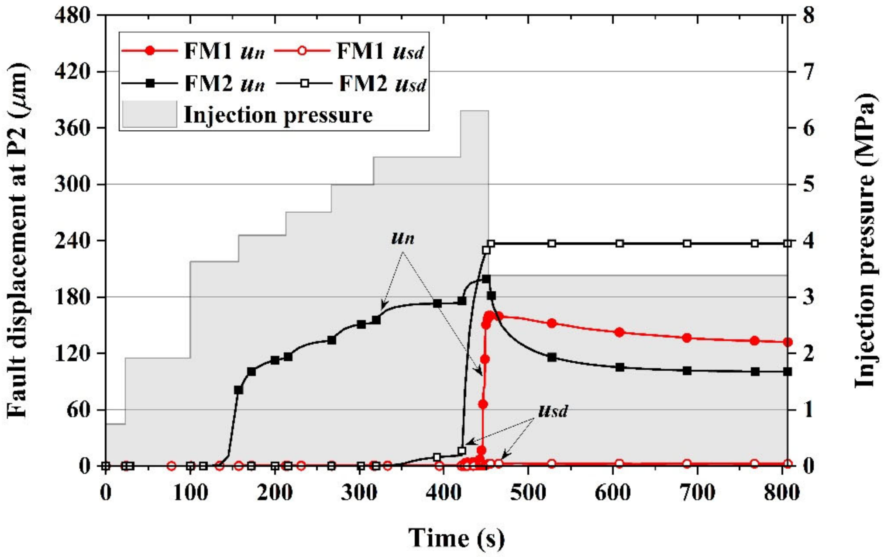

(b)

Fig. 11. Fault normal displacement (u_n) and fault shear displacement in the fault dip direction (u_{sd}) estimated at (a) P1 and (b) P2; the red lines denote the results of FM1 and the black lines denote the results of FM2.

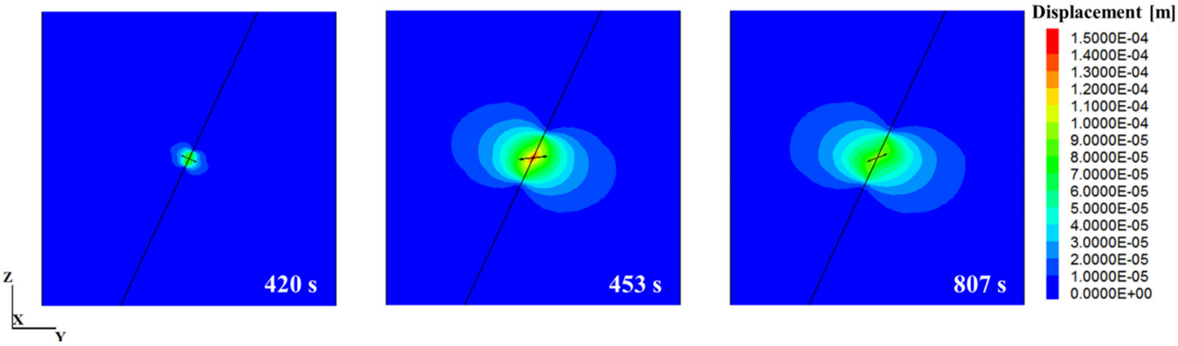

(a) FM1

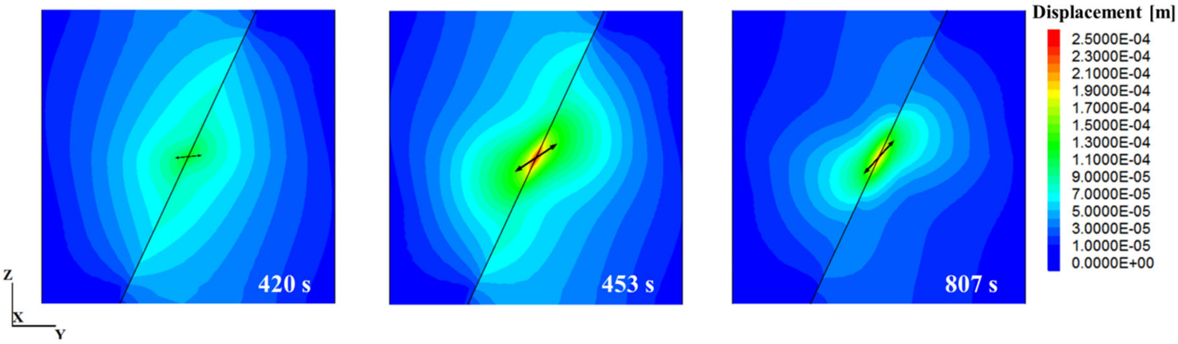

(b) FM2

Fig. 12. Rock displacement contours: (a) FM1 and (b) FM2; the scaled arrow denotes the fault displacement vector at injection point P1.

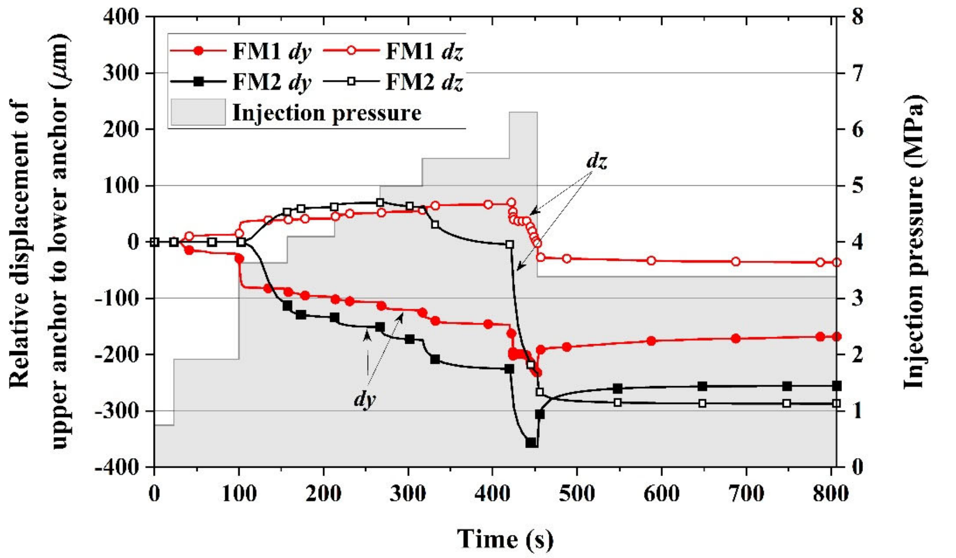

Fig. 13. Relative displacement of upper anchor to lower anchor; *dz* denotes the vertical displacement and *dy* denotes the displacement in the fault dip direction.

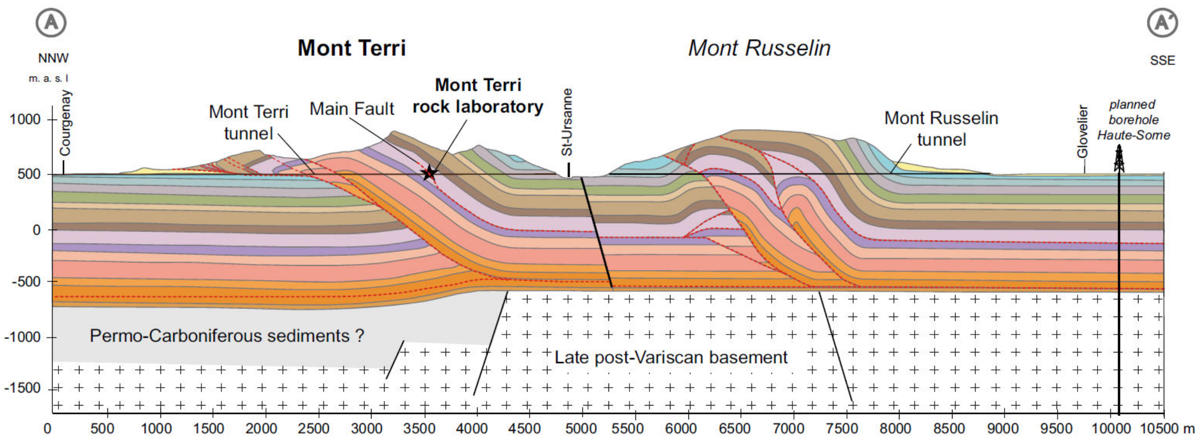

Fig. 14. Geological profile along the Mont Russellin and Mont Terri tunnels.[38]

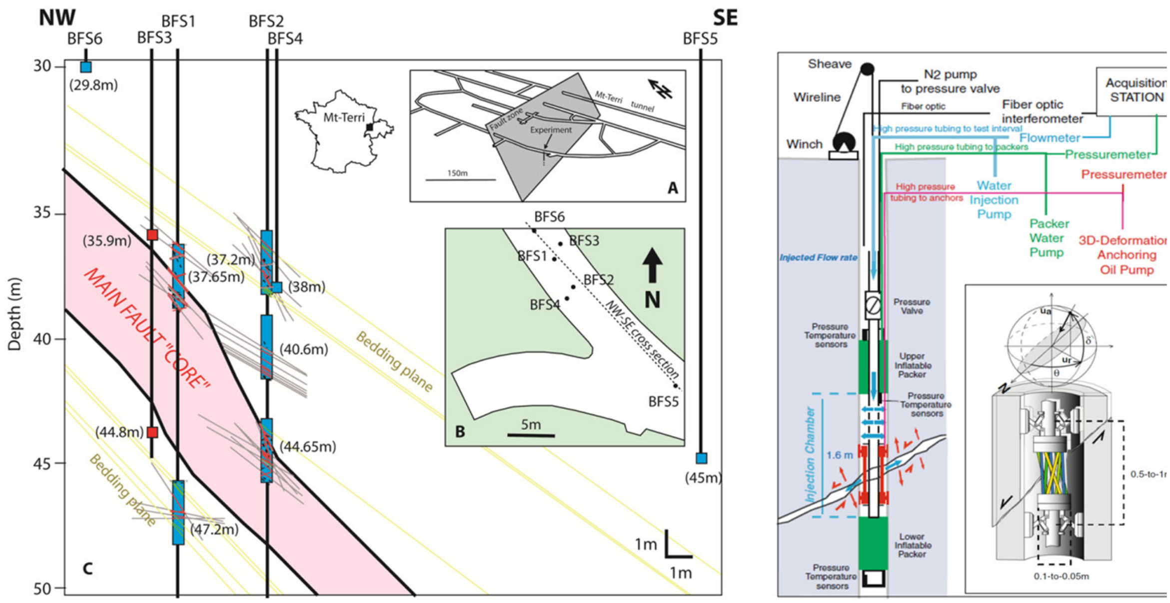

(a) (b)

Fig. 15. Mont Terri 'Main Fault' reactivation experiment[39, 40]: (a) fault plane with the injection location; (b) test equipment setup and deformation unit.

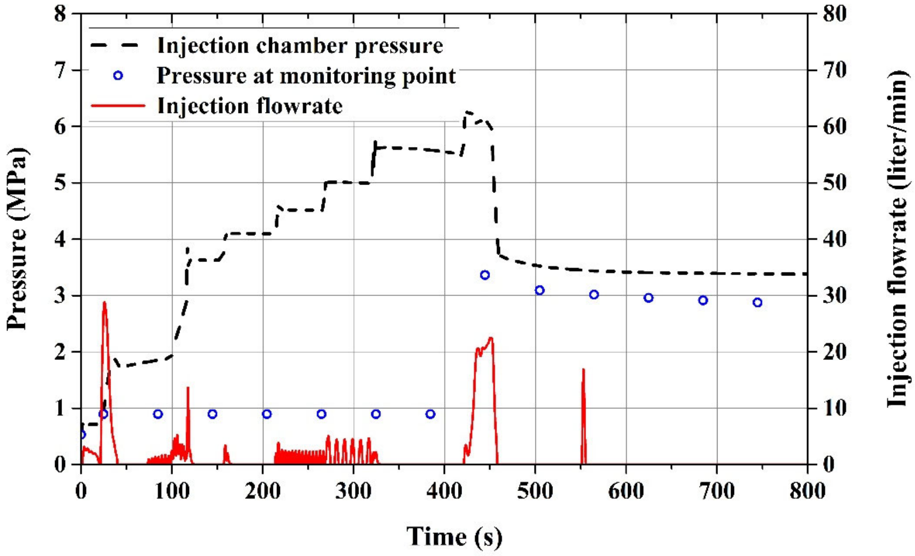

(a)

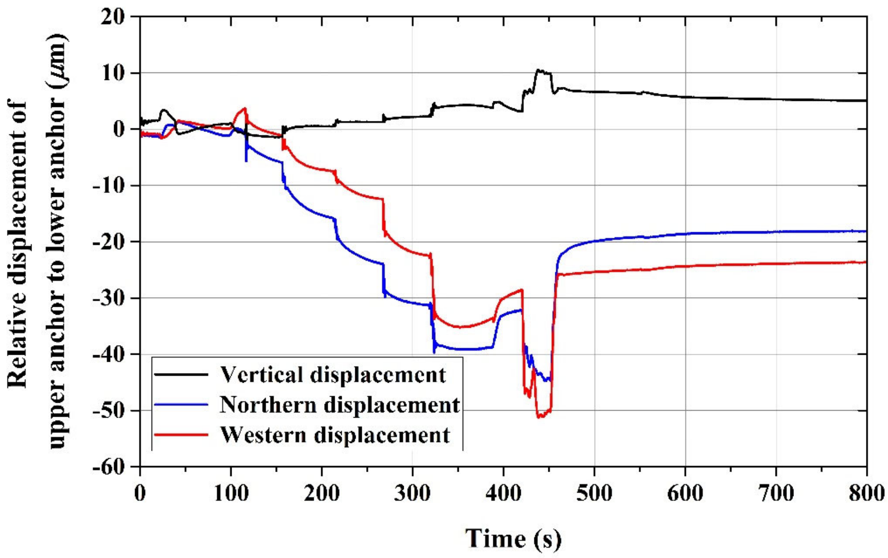

(b)

Fig. 16. Field experimental results for numerical simulation: (a) injection chamber pressure, pressure at monitoring point, and injection flow rate; (b) vertical and horizontal (northern and western) components of relative displacement of upper anchor to lower anchor.

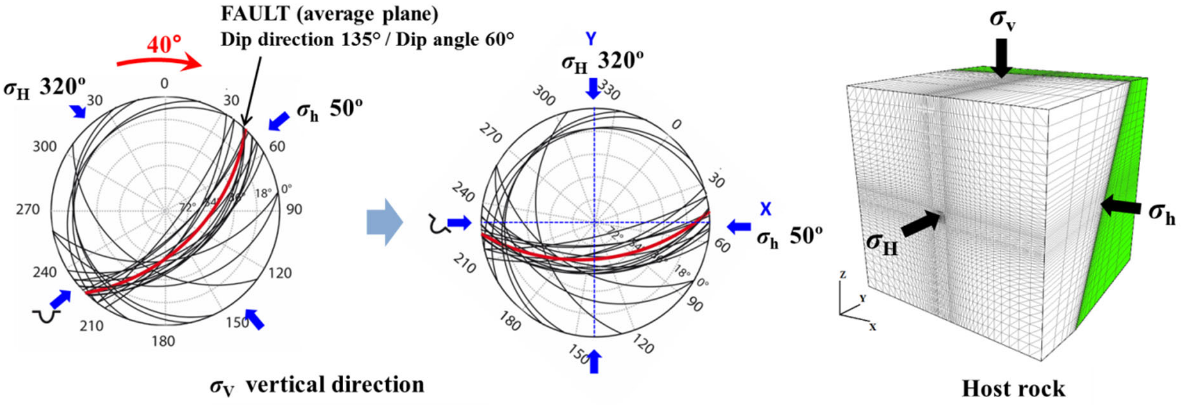

Fig. 17. Numerical model including a fault plane with a dip direction of 135º and dip angle of 60º.

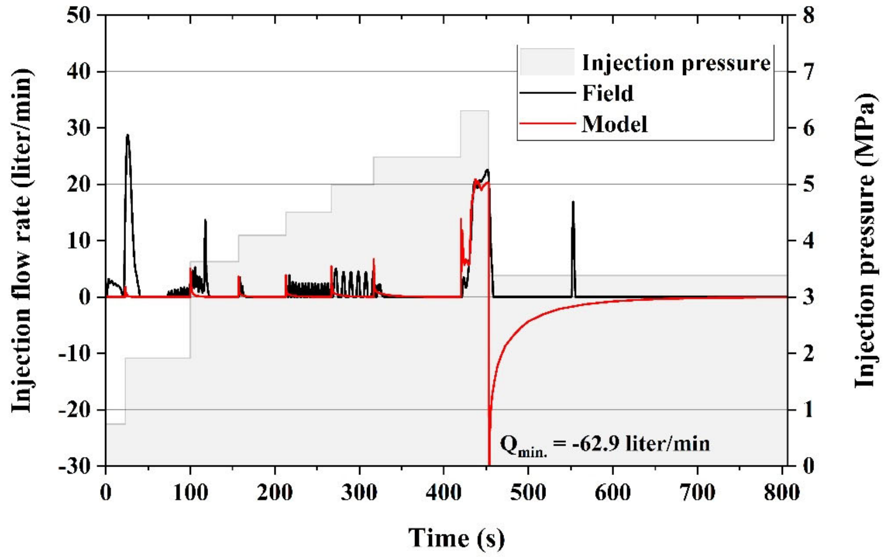

Fig. 18. Variation in injection flow rate (Case 1) – comparison between field experimental (black line) and numerical (red line) results.

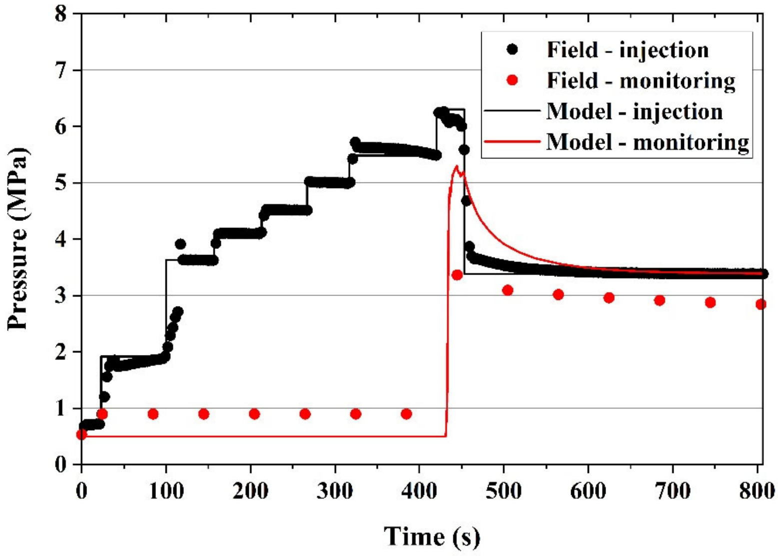

Fig. 19. Variations in pressures at injection and monitoring points (Case 1) – comparison between field experimental (dotted lines) and numerical (solid lines) results.

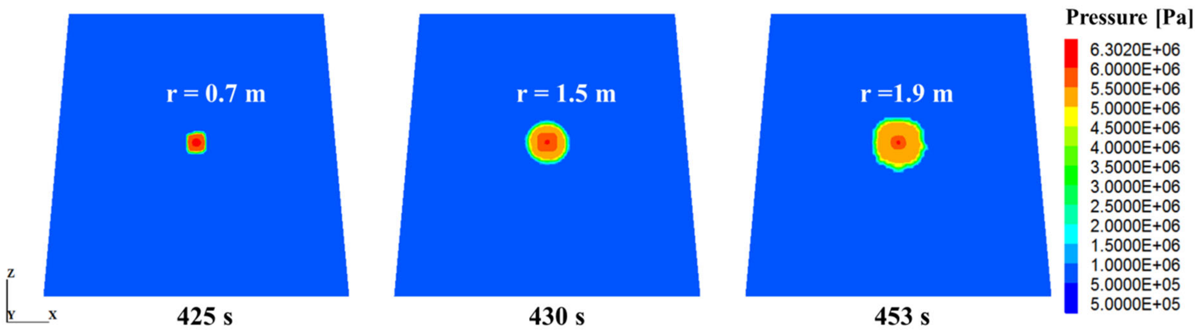

Fig. 20. Contours of pressure on the fault plane estimated at 425, 430, and 453 seconds (Case 1); *r* denotes the radius of the open fracture.

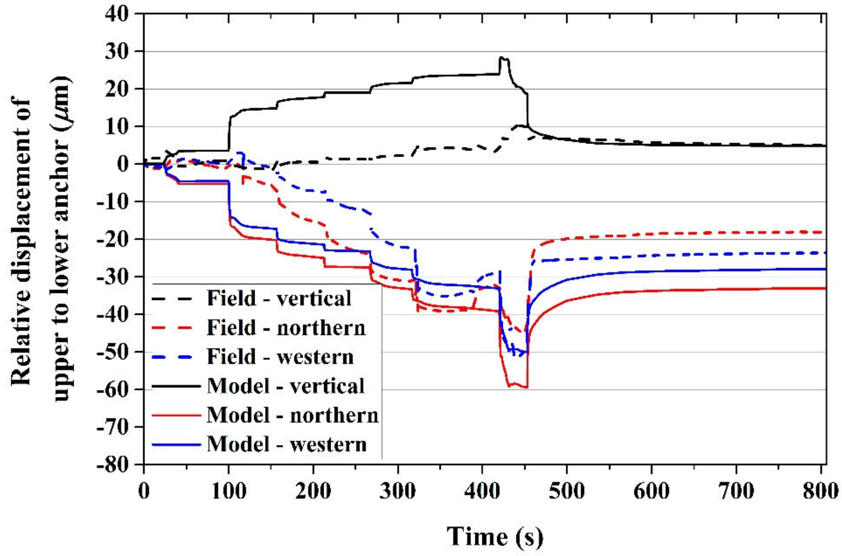

Fig. 21. Variations in relative displacement of upper anchor to lower anchor (Case 1) – comparison between field experimental (dashed lines) and best-matching numerical (solid lines) results.

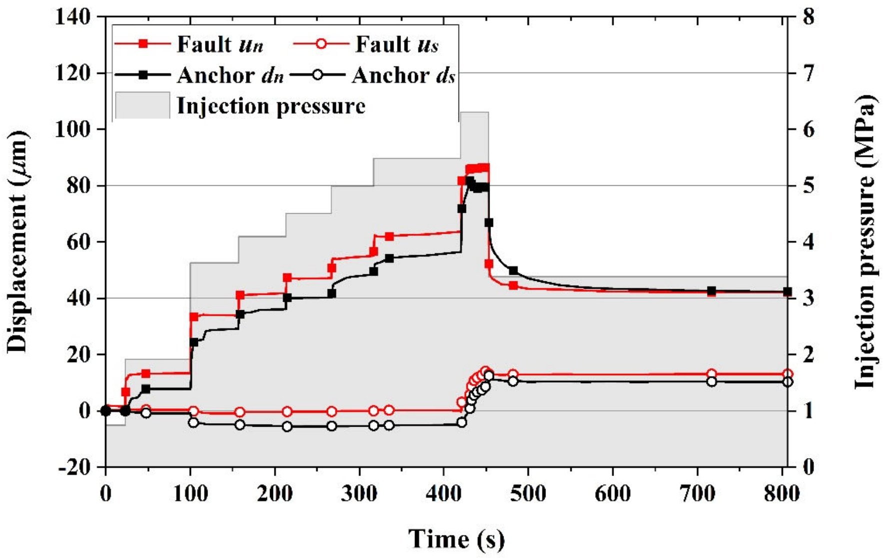

Fig. 22. Comparison between anchor displacement and fault displacement (Case 1); u_n and u_s denote the normal and shear displacements of the fault monitored at injection point P1; d_n and d_s denote the components of anchors' relative displacement vector in fault normal and shear directions.

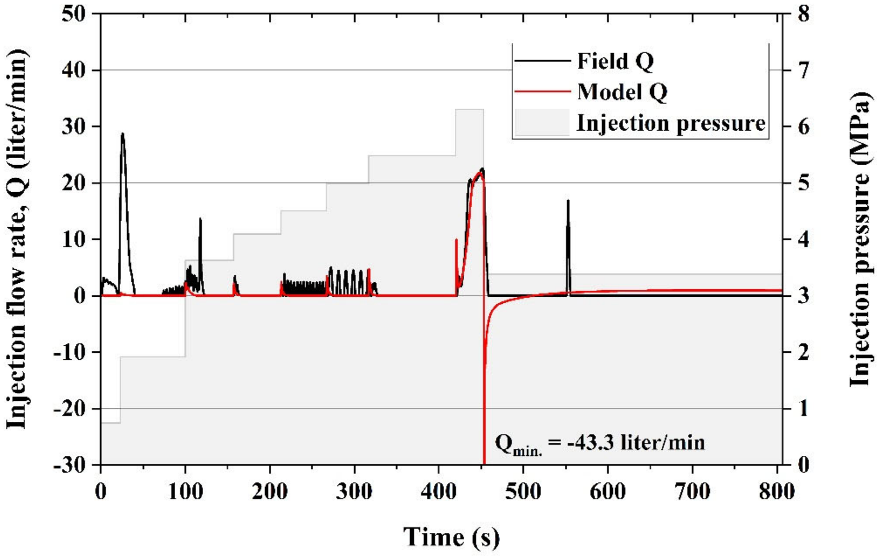

Fig. 23. Variation in injection flow rate (Case 2) – comparison between field experimental (black line) and numerical (red line) results.

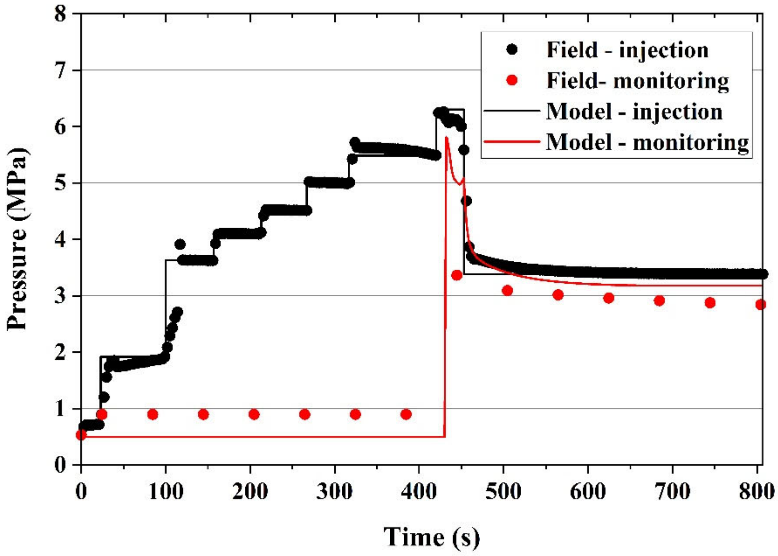

Fig. 24. Variations in pressures at injection and monitoring points (Case 2) – comparison between field experimental (dotted lines) and numerical (solid lines) results.

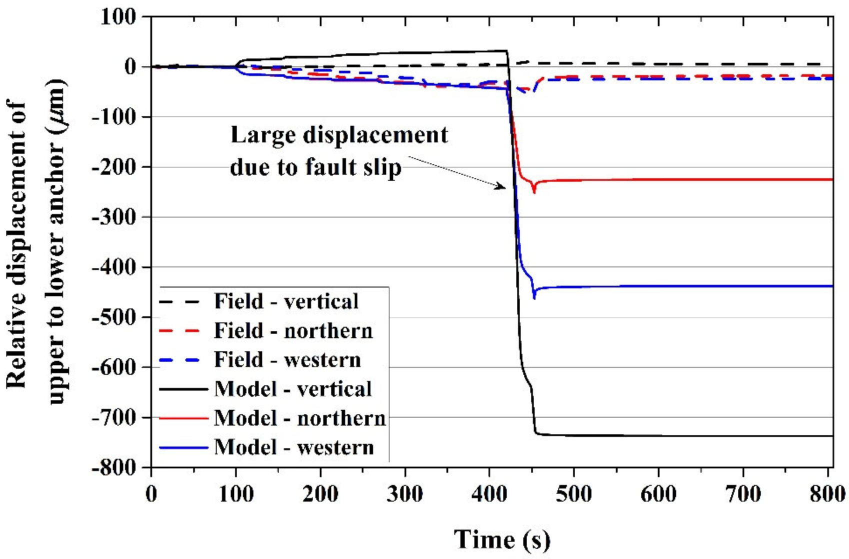

Fig. 25. Variations in relative displacement of upper anchor to lower anchor (Case 2) – comparison between field experimental (dashed lines) and numerical (solid lines) results.

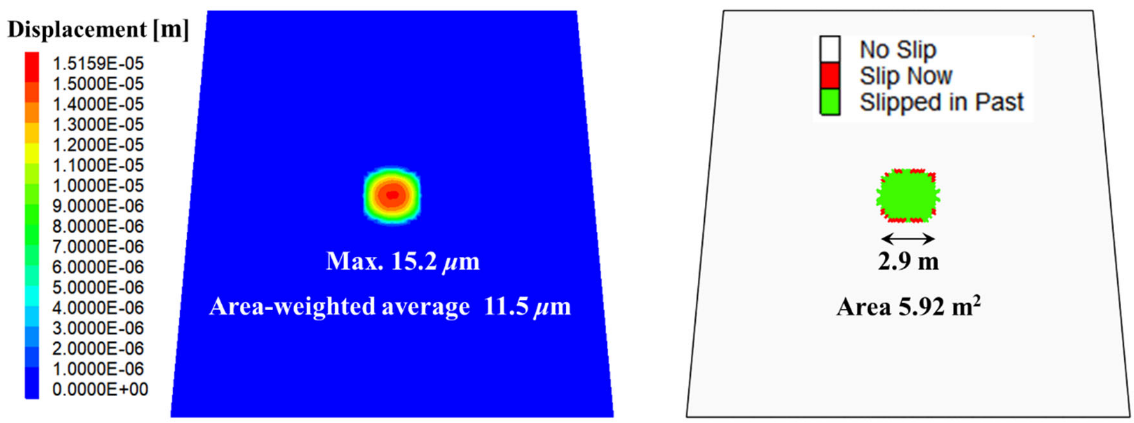

Fig. 26. Shear displacement and extent of shear failure zone estimated at 453 s of water injection with injection pressure of 6.302 MPa (Case 1)

Table 1. Input parameters of the host rock, fluid, and fault zone for benchmark calculations.

Material	Parameter	Value	
Host rock (Elastic)	Bulk modulus (GPa)	5.9	
	Shear modulus (GPa)	2.3	
	Bulk density (kg/m^3)	2450	
	Permeability	0	
Fluid	Density (kg/m^3)	1000	
	Compressibility (Pa^{-1})	4.4×10^{-10}	
	Dynamic viscosity (Pa s)	1.0×10^{-3}	
Fault (Elastic-perfectly plastic)	Fault model	FM1	FM2
	Normal stiffness (GPa/m)	20	20
	Shear stiffness (GPa/m)	20	20
	Cohesion (MPa)	0	0
	Static friction angle (º)	22	22
	Dilation angle (º)	0	10
	Tensile strength (MPa)	0	0
	Initial aperture (μm)	0	10
	Initial creation aperture (μm)	28	0

Table 2. Input parameters of fault and in-situ stress used for the calibration process.

Parameter		Range	Case 1 (Best match)	Case 2 (Second-best match)
Fault	Dip direction (º)	120 – 150	140	135
	Dip angle (º)	50–70	70	60
	Shear stiffness (GPa/m)	20–100	60	55
	Shear stiffness (GPa/m)	20–100	30	22
	Cohesion (MPa)	0–2	0	0.2
	Creation aperture at rupture (μm)	28–80	40	28
	Friction angle (º)	22 (Fixed)	22	22
	Dilation angle (º)	0 (Fixed)	0	0
	Tensile strength (MPa)	0 (Fixed)	0	0
In situ stress	Magnitude of principal stress (MPa)	$\sigma_1 = 5.0 – 7.0$ $\sigma_2 = 4.0 – 5.0$ $\sigma_3 = 0.6 – 3.0$	$\sigma_1 = 5.1$ $\sigma_2 = 5.0$ $\sigma_3 = 2.0$	$\sigma_1 = 7.0$ $\sigma_2 = 5.0$ $\sigma_3 = 3.0$